On the Formation of Adiabatic Shear Bands in Textured HCP Polycrystals

Zhen Zhang[1], Daniel E Eakins[2], and Fionn PE Dunne[1]

[1]Department of Materials, Royal School of Mines; [2]Institute of Shock Physics

Imperial College London, SW7 2AZ, London, United Kingdoms

Abstract

Adiabatic shear band (ASB) formation in textured HCP polycrystals has been investigated under regimes of high rate compression and shear loading using dynamic thermo-mechanically coupled, dislocation-based crystal plasticity modelling. The balance between rate of plastic dissipation leading to internal heat generation versus rate of thermal diffusion at a crystallographic length scale has been shown to be pivotal for the formation or otherwise of ASBs. Micro-texture has been found to have a key role in both advancing and inhibiting shear band growth, and its control offers the possibility of new alloys with higher impact strength over strain rate range 1×10^{-2} to 1×10^{5} s^{-1}. Texture has been found to lead to wide variations in applied macroscopic strain at which ASB formation occurs, such that strain level in isolation is inappropriate as a universal indicator of ASB onset.

High-rate shear loading is found to lead to lower onset strains for ASBs compared to high rate compression, but the dependence of both on texture leads to considerable variation in strain level for ASB formation. A preliminary map demarcating ASB onset has been established over regimes of applied strain and texture for dynamic shear and compression.

Keywords: Adiabatic shear band, micro-texture, HCP polycrystals, impact, strain rate sensitivity, internal heat generation, thermo-mechanical instability

1. Introduction

Adiabatic shear band (ASB) formation remains an important phenomenon in a range of technological and industrial application areas, including that of foreign object damage in aero-engines. It is a highly complex process involving dynamic deformation, high-rate plasticity, internal heat generation, thermal transients with big local temperature excursions, and very localised slip. An area of research which has received limited attention in this context is microstructure and texture. Hence, the primary aim of this paper is to address the role of crystallographic texture, and local micro-texture, on ASB formation, with the objective of establishing whether good or bad textures, or carefully contrived micro-textures, could be utilised to control, and therefore inhibit, ASB formation.

Localized heating during plastic deformation was first observed by Tresca (1878) in his forging experiment on iron, and Basinski (1957) found that the resulting localized temperature rise could cause measurable discontinuities in the corresponding stress-strain curve. In fact, the temperature rise can be sufficient to heat the material so as to produce unstable, highly localised conditions of plastic flow. More often than not, the localisation phenomenon is associated with dynamic high strain-rate loading, such as that encountered during impact, and shear bands are found to develop and propagate quickly through the material and are often followed immediately by fracture. The short loading duration acts to inhibit the local heat conduction, which in turn is argued to be a contributory factor in ASB formation by virtue of highly localised temperature increases, enhancing local softening, potentially followed by void growth and failure (Wright, 2002), in particular for materials with low coefficient of thermal conductivity, low specific heat, and high density (Antolovich and Armstrong, 2014). It is thus reasonably difficult to find ASBs in copper where the material's high thermal conductivity is sufficient to conduct heat away from localisation regions.

The concentration of plastic work within discrete bands results in far more extreme load conditions then throughout the bulk. Local plastic strains in the bands can be as high as 10-10^2, with associated strain rates of 10^5 - 10^7 s^{-1} (Guduru et al., 2001a). In the ASB region formed by impacting the Ti-6Al-4V alloy (Liao and Duffy, 1998), the local strain rate has been reported to be around 8×10^4 s^{-1} under a nominal/global strain rate of 10^3 s^{-1}. The local strain could be surprisingly high from about 0.75 to 3.50. The local strain rate is above 1×10^4 s^{-1} in the ASBs associated with metal machining when the nominal strain rate is about 10^3 s^{-1} (Childs, 2014). In Split Hopkinson Pressure Bar (SHPB) experiments, typical loading strain rates are 10^4 s^{-1}. Strain rates from 10^4 s^{-1} to 10^8 s^{-1} are achievable by Taylor impact/plate impact, where uniaxial stress states are not possible to obtain (Field et al., 2004; Ramesh, 2008).

For Ti-6Al-4V, the shear bands range from 10-50 μm in width (Coghe et al., 2006; Liao and Duffy, 1998; Meyers and Pak, 1986), which is argued to be determined by the thermal diffusivity (Merzer, 1982), and the characteristic length scale is of the order of $\sqrt{\alpha t}$ where α is the thermal diffusivity of the material, and t is the loading duration (Chichili et al., 2004; Childs, 2014). The ASB band width is found to increase nonlinearly with shear strains, for example 10 μm, 15 μm, and 18 μm for 2.5, 3.5, and 8 global strain, respectively, leading to band width saturation at 20 μm (Meyers et al., 1994).

ASB temperature distributions are known to be highly transient, with short range spatial periodicity in the direction of their growth (Guduru et al., 2001a). The temperature has been measured by Ranc et al. (2008) separately for initiation and propagation of ASBs in Ti-6Al-4V during dynamic torsion testing. With a global strain rate from 1000 s^{-1} to 2000 s^{-1}, the low temperature range for ASB initiation is found to be from 50°C to 300°C and the high temperature range for ASB propagation from 800°C to 1700°C. Temperature heterogeneity,

i.e. highly non-uniform with discrete regions of high temperature, is observed along the formation length of ASBs. This has also been found by Guduru et al. (2001b) based on high-speed infrared camera measurement.

It has been noted by Ranc et al. (2008) that the difficulty of accurately capturing the ASB formation lay in achieving simultaneously high resolutions in time, space and temperature measurement. For instance, it is difficult to simultaneously maintain a temporal resolution of about 1 μs and spatial resolution of 43 μm for low temperature ranges and 10 μs and 2 μm respectively for the high temperature range. Continuous and high-speed temperature measurement from 50°C to 1670°C (melting point of Ti-6Al-4V) remains very difficult for a single pyrometer. This has hindered a better understanding of the onset mechanisms in shear localization and formation of ASBs.

The mechanisms of ASB formation remains controversial (Medyanik et al., 2007; Peirs et al., 2013; Rittel, 2009). Conventional criteria for the initiation of ASBs are to define a critical shear strain (Zhou et al., 1996a). Nevertheless, for a given shear stress, the critical strain decreases with increasing strain rate (Lindholm, 1974) and this is attributed to the increase in strength at high strain rates (Meyers, 1994). Weak strain-rate sensitivity characterised by small rate hardening exponent reduces the strain necessary for the onset of shear bands (Clifton et al., 1984). On the other hand, shear localization can be delayed by the effects of strain hardening (Clifton et al., 1984). Nonetheless, ASBs are commonly considered as an instability resulting from thermal softening effects (Bai and Dodd, 2012; Wright, 2002). In order to understand the emergence of an adiabatic shear band, Zener and Hollomon (1944) proposed to consider the competing influence of strain-rate hardening and thermal softening effects, the latter generating conditions where the material can no longer harden, thus losing its stability and allowing the formation of a localized failure mode.

Internal heat generation is recognized to be important for nucleation of adiabatic shear banding, and has been considered in the classical Johnson-Cook model (Chen and Ghosh, 2012; Dolinski et al., 2010; Khan et al., 2004), the Kocks-Mecking model (Chichili et al., 1998; Follansbee and Gray III, 1989), continuum viscoplasticity models (Rosakis et al., 2000; Zhou et al., 1996a; Zhou et al., 1996b), and crystal plasticity models (Austin and McDowell, 2011; Clayton, 2005; Lloyd et al., 2014a; Lloyd et al., 2014b). Most of these investigations are concerned with the macroscopic stress, strain and strain rate. Among these numerical methods, the crystal plasticity models provide promise in linking the macroscopic mechanical behaviours with their microstructural origins. The microstructural mechanisms are argued to be dominated by dislocations when the applied strain rate is less than 10^4 s^{-1} (Austin and McDowell, 2011; Gilat and Clifton, 1985; Khan et al., 2004)

An important aspect of microstructure relevant to ASB formation but which has yet to receive significant attention is that of the effect of crystallographic texture, together with that of grain size distribution. Researchers have argued that the stored energy of cold work is significant (Rittel, 2009; Sun et al., 2014), potentially through its influence on local slip strength and localisation; coarse-grained microstructures lead to low stored energy and ultra-fine-grained microstructures give rise to high stored energy. The importance of initial crystal orientation/texture has also been noted in studies of wave propagation and dynamic response of single and polycrystal aluminium. Lloyd et al. (Lloyd et al., 2014a) studied high rate single crystal response of aluminium with a peak pressure below 30GPa, and showed that initial crystal orientation played a significant role in both wave propagation profile and microstructure evolution in FCC metals. They considered initial orientations of five hundred randomly oriented crystals, and their results revealed that for below 5 GPa pressures, a slight orientation dependence was found since the response is governed by dislocation multiplication. The orientation dependency increased with increasing pressure from 5 to 15

GPa for which the primary dislocation generation mechanism transitioned from dislocation multiplication to heterogeneous nucleation. When the shock pressure increased from 15 to 25 GPa, the orientation dependencies decreased as the homogeneous dislocation nucleation dominates the plastic deformation mechanisms. Lloyd et al. (2014b) found that the initial material heterogeneity significantly affected the high strain rate dynamic responses in aluminium, with peak shock pressure up to 110 GPa. For HCP metals, Coghe et al. (2006) tested Ti-6Al-4V SHPB cylindrical samples, and found that the deformation mechanism transition zone is strongly influenced by texture. As demonstrated in their results, the deformation is dominated by generalised slip at a strain rate less than 0.5 s^{-1}, then a transition zone exists with combined ASB and general slip from a strain rate up to 10 s^{-1}. At even higher strain rate, adiabatic shear banding was found to be the major deformation mechanism observed. Peirce et al. (1982) in crystal modelling studies found that the pattern of shear banding depended on the initial geometric imperfection, but also on the size of the imperfection to a critical size below which the dependence ceased. Schoenfeld and Kad (2002) reported differing shear band patterns in highly oriented and random textured Ti-6Al-4V under simple shear. Mayeur and McDowell (2007) noted that transverse and basal/transverse textured Ti-6Al-4V polycrystals displayed markedly different stress-strain behaviour when loaded in the texture TD direction. Kuroda and Tvergaard (2007) studied the effects of the typical five texture components on shear band development investigated for plane strain tension/compression and bending problems, using crystal plasticity simulations on rolled aluminium alloy sheets. Cube texture was found to be very advantageous for preventing shear band development. Clayton (2009) showed that specific aspects of microstructure were important in shear localization, including random and rolled cubic textures as well as stored elastic energy and residual volume changes associated with lattice defects, impurities, and inclusions such as second phases in the metal-matrix.

The aim of the present work is to study the role of initial texture on the dynamic response and adiabatic shear banding in HCP polycrystals, employing Ti-6Al as a model alloy. The methodology is to utilise dislocation-based crystal plasticity enhanced to incorporate internal heat generation, fully thermo-mechanically coupled within a dynamic finite element formulation. The study addresses textured polycrystals subjected to loading from the quasi-static rate up to high rates associated with impact, with the objective of quantifying the rate-dependence of the onset of ASB formation, by determining the strain at which initiation occurs for a given strain rate. The study is carried out over a range of textures also, such that it begins to become possible to establish deformations maps over texture, loading rate and level of deformation for which ASB formation occurs. This remains a key technological challenge in a range of safety-critical applications, and the establishment of such maps may facilitate the optimisation of materials and textures for some high-demand applications particularly relevant to aerospace applications.

In the following sections, the thermo-mechanically coupled energy formulation is presented, followed by the dislocation-based crystal plasticity model with internal heat generation. Model representation of HCP polycrystals under dynamic loading is then described, together with the incorporation of polycrystal texture. There then follows the presentation of a systematic study of load-up rate, pulse duration, and texture in HCP polycrystals, and in particular, an examination of the onset of ASB formation, and its dependence on strain level, loading rate, and texture. We include an assessment of the role of local micro-texture in inhibiting or otherwise shear band formation, and present a summary of high-rate deformation maps relevant to ASB development.

2. Thermo-mechanical crystal plasticity formulation with internal heat generation

We begin by assuming adiabatic conditions, wherein there is no transfer of heat between our polycrystal and its surroundings and there is no external heat source. The problem is thus represented by fully coupled thermo-mechanical dynamic deformation with internal heat generation, and the governing equations are therefore prescribed by the principle of virtual work and adiabatic heat transfer.

The variation in virtual work gives

$$\int_{\overline{V}} \rho \ddot{\mathbf{u}} \delta \mathbf{u} d\overline{V} + \int_{\overline{V}} \boldsymbol{\tau} \delta \mathbf{E} d\overline{V} - \int_{\overline{V}} \mathbf{f} \delta \mathbf{u} d\overline{V} = 0 \tag{1}$$

where $\overline{V}$ represents the volume of the body in the reference configuration, ρ is the initial mass density, $\boldsymbol{\tau}$ the second Piola Kirchhoff stress, $\mathbf{E}$ the Green-Lagrangian strain, $\mathbf{f}$ is the volume density body force, $\mathbf{u}$ the displacement and $\ddot{\mathbf{u}}$ the acceleration.

The variational form of adiabatic heat transfer but with internal heat generation through plastic dissipation is given by

$$\int_{\overline{V}} \rho c_P \dot{\Theta} \delta \Theta d\overline{V} - \int_{\overline{V}} k \nabla \Theta \nabla \delta \Theta d\overline{V} - \int_{\overline{V}} \beta \sigma_{eff} \dot{p} \delta \Theta d\overline{V} = 0 \tag{2}$$

where c_P is the specific heat, Θ the temperature, and k the heat conductivity. The quantity $\sigma_{eff} = \sqrt{\frac{3}{2}\boldsymbol{\sigma}' : \boldsymbol{\sigma}'}$ is the von Mises effective stress where the stress deviator is given by $\boldsymbol{\sigma}' = \boldsymbol{\sigma} - \frac{1}{3} tr(\boldsymbol{\sigma})\mathbf{I}$. The effective plastic strain is given in terms of the plastic deformation gradient by $\dot{p} = \sqrt{\frac{2}{3}\mathbf{D}^p : \mathbf{D}^p}$ where $\mathbf{D}^p = sym(\mathbf{L}^p)$ and where $\mathbf{L}^p$ is the plastic velocity gradient detailed in the following section. The quantity β represents the fraction of plastic work converted to heat, often referred to as the Taylor-Quinney coefficient (Taylor and Quinney, 1934). For simplicity we take a value of 0.9 in this study, but this is discussed

further in a later section in relation to experimental methodologies under development for its determination. However, as shown by previous works on titanium alloys, this choice has been shown to lead to reasonable temperature rise measurements (Follansbee and Gray III, 1989; Khan et al., 2004; Meyers et al., 1994).

The boundary integrals are ignored since all internal heat is assumed to be generated from the plastic dissipation within the volume, there are no external heat sources, and there is no heat dissipation to the outer environment through the surfaces of the considered volume. These assumptions are reasonable for modelling of ASB formation since relevant experimental data show that the onset and development of ASBs is a transient and high-rate event occurring over a time scale of tens of microseconds (Peirs et al., 2013; Ranc et al., 2008).

Therefore the weak form of coupled equilibrium given in Eqs. (1) and (2) with the assumptions stated may be re-written as

$$\rho\ddot{\mathbf{u}} - div\boldsymbol{\sigma} - \mathbf{f} = 0 \tag{3}$$

and

$$\rho c_P \dot{\Theta} = \beta\sigma_{eff}\dot{p} + div(k\nabla\Theta) \tag{4}$$

Note that under strictly adiabatic conditions where localized heat transfer is inhibited, within the neighbourhood of a material point, Eq. (4) can be reduced such that

$$\dot{\Theta} = \frac{\beta\sigma_{eff}\dot{p}}{\rho c_P} \tag{5}$$

Eq. (5) is indicative of the temperature evolution during adiabatic ASB formation, but in fact full thermo-mechanical coupling given by Eq. (4) is included. The thermoelastic coupling is

neglected because of it is argued to be small with respect to the internal heat generation resulting from plastic dissipation. However, the full representation may be found in Wright (2002) or Clayton (2010), in which formulations applicable for general thermo-mechanical coupling effects are given.

2.1 Kinematics

The deformation gradient is decomposed into elastic and plastic parts, such that

$$\mathbf{F} = \mathbf{F}^e \mathbf{F}^p \mathbf{F}^\Theta \tag{6}$$

where $\mathbf{F}^e$ denotes small elastic stretches and arbitrary rigid-body rotations. $\mathbf{F}^\Theta$ represents the thermally-expanded unstressed configuration (Meissonnier et al., 2001). $\mathbf{F}^p$ evolves based on the flow rule as

$$\dot{\mathbf{F}}^p = \mathbf{L}^p \mathbf{F}^p \tag{7}$$

where $\mathbf{L}^p$ is the plastic velocity gradient. In the crystal plasticity formulation, $\mathbf{L}^p$ comprises the summed resolved crystallographic plastic slip rates $\dot{\gamma}^\alpha$, such that

$$\mathbf{L}^p = \sum_\alpha \dot{\gamma}^\alpha \mathbf{s}^\alpha \otimes \mathbf{n}^\alpha \tag{8}$$

where $\mathbf{s}^\alpha$ and $\mathbf{n}^\alpha$ are respectively the slip direction and slip plane normal on the α-th slip system with respect to the reference configuration.

The dislocation-based slip rule employed is given by

$$\dot{\gamma}^\alpha = \rho_m v b^2 \exp\left(-\frac{\Delta H}{k\Theta}\right) \sinh\left[\frac{(\tau^\alpha - \tau_c^\alpha)\gamma_0 b^2}{k\Theta\sqrt{\rho_o}}\right] \tag{9}$$

where ρ_m is the density of mobile dislocations, ν the frequency of attempts of dislocations to jump energy barriers corresponding to dislocation obstacles, b the Burger's vector magnitude, ΔH the activation energy for self-diffusion, and k the Boltzman constant. τ^α represents the resolved shear stress on slip system α, and τ_c^α is the slip strength or critical resolved shear stress. Θ is the temperature, and γ_0 a representative shear strain magnitude conjugate to the local resolved shear stress. The origin and details of the slip rule may be found in Dunne et al. (2007). The density of statistically stored dislocations, ρ_o, is prescribed to evolve with local accumulated slip according to

$$\dot{\rho}_o = \gamma' \dot{p} \tag{10}$$

where γ' is a hardening parameter ascribed to grain boundary interaction effects such that it is nonzero only in the case of polycrystals. This is to account for the hardening effect due to the grain boundaries in polycrystals.

The slip strength hardening is given by

$$\tau_c^\alpha = \tau_{c0}^\alpha(\Theta) + G(\Theta) b \sqrt{\rho_o} \tag{11}$$

in which $\tau_{c0}^\alpha(\Theta)$ and $G(\Theta)$ are the temperature dependent critical resolved shear stress and shear modulus, respectively. The temperature dependencies of material parameters are given in Appendix A. The slip systems in the HCP unit cell are shown in Figure 1. Note that basal and prismatic slip systems are found to have similar slip strengths τ_{c0} at room temperature. The slip strength of pyramidal slip systems is found to be about three times that of basal/prismatic systems (Gong and Wilkinson, 2009).

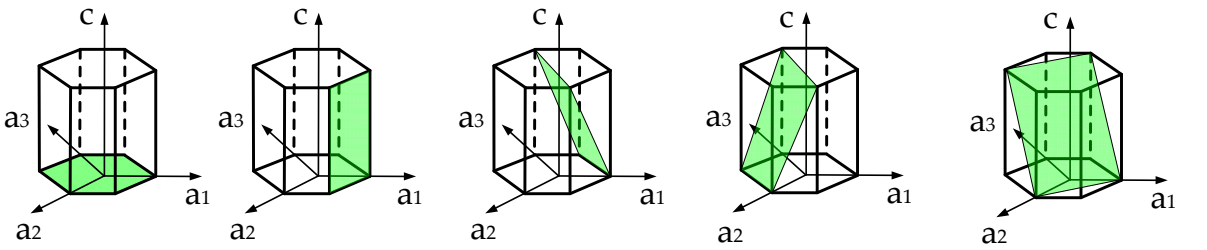

(a) Basal <a>, 3 **(b)** Prismatic <a>, 3 **(c)** Pyramidal <a>, 6 **(d)** 1st Order Pyramidal <c+a>, 12 **(e)** 2nd Order Pyramidal <c+a>, 6

Figure 1 Slip systems in an HCP single crystal

The resolved shear stress τ^{α} on slip system α is given by

$$\tau^{\alpha} = \boldsymbol{\sigma}\mathbf{n}^{\alpha} \cdot \mathbf{s}^{\alpha} \tag{12}$$

which is utilised in conjunction with Schmid's rule to determine if the given slip system is active or otherwise. If so, the symmetric part of the plastic velocity gradient $\mathbf{L}^{p}$ provides the plastic deformation gradient $\mathbf{D}^{p} = sym(\mathbf{L}^{p})$ and the antisymmetric part the plastic spin. The Jaumann stress rate is determined from the elastic rate of deformation given by

$$\overset{\nabla}{\boldsymbol{\sigma}} = \mathbf{C} : (\mathbf{D} - \mathbf{D}^{p} - \mathbf{D}^{\Theta}) \tag{13}$$

where $\mathbf{C}$ is the elastic stiffness, and $\mathbf{D}$ and $\mathbf{D}^{\Theta}$ are the total and thermal rates of deformation respectively.

The thermal rate of deformation is given by

$$\mathbf{D}^{\Theta} = \mathbf{R}\boldsymbol{\alpha}\mathbf{R}^{-1}\dot{\Theta} \tag{14}$$

in which $\boldsymbol{\alpha}$ is the anisotropic thermal expansivity, here written in matrix form, recognising its anisotropic nature in HCP crystals, such that $\boldsymbol{\alpha} = diag\left[\alpha_a \quad \alpha_a \quad \alpha_c\right]$ in which the subscripts a and c correspond to the associated HCP single crystal directions respectively, and the

magnitudes are obtained from Pawar and Deshpande (1968) and are given in Appendix A. The formulation of the rotation matrix $\mathbf{R}$ comes from knowledge of the crystallographic orientation of individual grains and is given in Appendix B.

The global elastic stiffness matrix $\mathbf{C}$ can be determined from the local anisotropic crystal stiffness matrix from the transformation

$$\mathbf{C}' = \mathbf{T}_{\sigma}^{-1}\mathbf{C}\mathbf{T}_{\varepsilon} \tag{15}$$

where the transformation matrices $\mathbf{T}_{\sigma}$ and $\mathbf{T}_{\varepsilon}$ can be derived from the rotation matrix $\mathbf{R}$. The inverse matrix of $\mathbf{T}_{\sigma}$ and $\mathbf{T}_{\varepsilon}$ are represented in Voigt notation in terms of 6×6 rotation matrices. The local stiffness matrix $\mathbf{C}$ is an elastic anisotropic matrix, given for alpha titanium in, eg, Dunne et al. (2007) .

The consistent tangent stiffness matrix is also given by Dunne et al. (2007) as

$$\mathbf{D} = (\mathbf{I} + \mathbf{C}'\mathbf{P})^{-1}\mathbf{C}' . \tag{16}$$

The matrix $\mathbf{P}$ is contributed by the crystal slip and it may be expressed as

$$\mathbf{P} = \sum_{\alpha} \eta\xi \cosh\xi(\tau^{\alpha} - \tau_c)\mathbf{A}^{\alpha} \otimes \mathbf{A}^{\alpha} \tag{17}$$

where $\mathbf{A}^{\alpha}$ is a 6×1 vector determined by $\mathbf{s}^{\alpha}$ and $\mathbf{n}^{\alpha}$ (Dunne et al., 2007). When $\tau^{\alpha} < \tau_c$, there is no contribution from $\mathbf{P}$, and the $\mathbf{D}$ matrix reduces to the elastic tangential modulus matrix $\mathbf{C}'$.

Based on Eq. (9), it is found that η and ξ in Eq. (17) are such that

$$\eta = \rho_m \nu b^2 \exp\left(-\frac{\Delta H}{k\Theta}\right) \tag{18a}$$

$$\xi = \frac{\gamma_0 b^2}{k\Theta\sqrt{\rho_o}} \tag{18b}$$

The crystal plasticity model for this study is implemented into an ABAQUS VUMAT within a fully coupled 3D thermo-mechanical element formulation, thus facilitating the incorporation of internal heat generation from the local plastic dissipation and solution of the transient heat transfer problem, within an ABAQUS explicit dynamic finite element formulation.

3. Systematic study of rate, deformation and texture on ASB formation

In examining the formation of adiabatic shear bands in HCP polycrystals, we wish to differentiate the contributions, if possible, from wave propagation, strain accumulation, strain rate, and softening induced by internal heat generation, and importantly, polycrystal texture. The polycrystal model boundary and loading conditions are described first.

3.1 Polycrystal model, boundary conditions and loading

Figure 2 shows the schematic diagram of the model polycrystal with dimensions 200 x 200 x 20 μm chosen to investigate ASB development in, and to be representative of both SHPB compression experiments and top-hat shear sample experiments (Meyers et al., 1994). Considering the dimensions of the polycrystal specimen selected and shown in Figure 2(a), the loading velocity is chosen to range from quasi-static conditions, with a strain rate of 0.01 s^{-1}, through to dynamic behaviour, with a strain rate of 1×10^5 s^{-1} (eg. v_{peak}=20 m/s). This loading velocity range selected allows a full study of the deformation from static to dynamic cases. The dynamic load is imposed with velocity boundary condition with a rise time of t_r, as shown in Figure 2(a). The finite element model representation of the polycrystal is shown

in Figure 2(b). The model is meshed with 25,088 ABAQUS C3D8RT three-dimensional, thermally-coupled continuum elements with a minimum of nine in-plane elements within a 10 μm by 10 μm region of area, compatible with that adopted in other studies (Clayton, 2005; Dolinski et al., 2010; Liao and Duffy, 1998). A simplification in the present study is to utilise grains with hexagonal morphology, and while fully three-dimensional crystallographic orientations and crystal slip are facilitated, the grains considered are pseudo-3D in the sense of being prismatic through the polycrystal depth, as shown in Figure 2(b). Both dynamic uniaxial compression and shear are considered as shown in Figure 2(c) and (d), so as to study the relationship between loading type and ASB failure mode in the range of polycrystal textures considered. Periodic boundary conditions are imposed in order to be representative of a polycrystal morphology and texture.

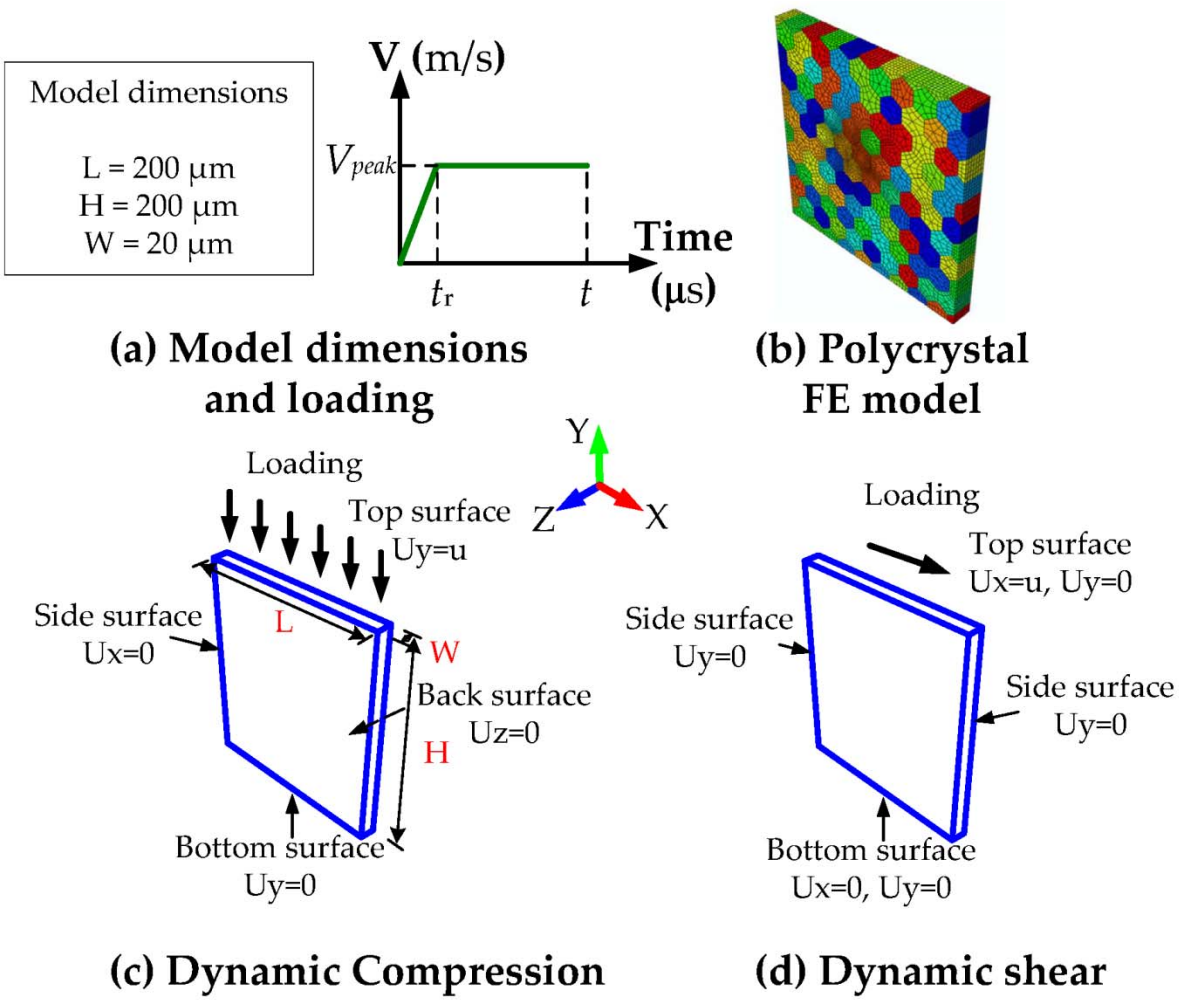

Figure 2 Model dimensions, finite element representation, and boundary conditions and applied dynamic loading

3.2. Preliminary study of single and polycrystal response under dynamic loading

As a preliminary study, HCP single and polycrystal responses to uniaxial dynamic compression loading are considered first, and the velocity boundary conditions defining rise time and maximum applied velocity (20 ms^{-1}) imposed are shown in Figure 3, together with the single crystal orientation, and polycrystal texture. The texture employed for the polycrystal is generated to give an in-plane random crystal orientation with the crystal c-axes close to parallel to the z axis for most grains. The quantitative measure of this texture is given by the Kearn's factors in Table 1. The results obtained showing both the onset of shear

band formation (for the strains of 4.6% and 4.5% for the single and polycrystal samples respectively) and at the point of collapse (for strains of 8.5% and 7.2% respectively) are also given in Figure 3. The onset of shear band formation is shown in Figure 3(b) and (e), and the point of collapse in each in Figure 3(c) and (f), respectively. For the single crystal, the onset of ASB formation occurs at the top right boundary of the specimen and the shear localization develops along prism slip planes until it reaches the other boundary of the specimen. During the initiation of the ASB in the single crystal specimen, wave propagation is the predominant nucleation source because of the heterogeneous deformation it generates since its wave length is small compared to the sample size.

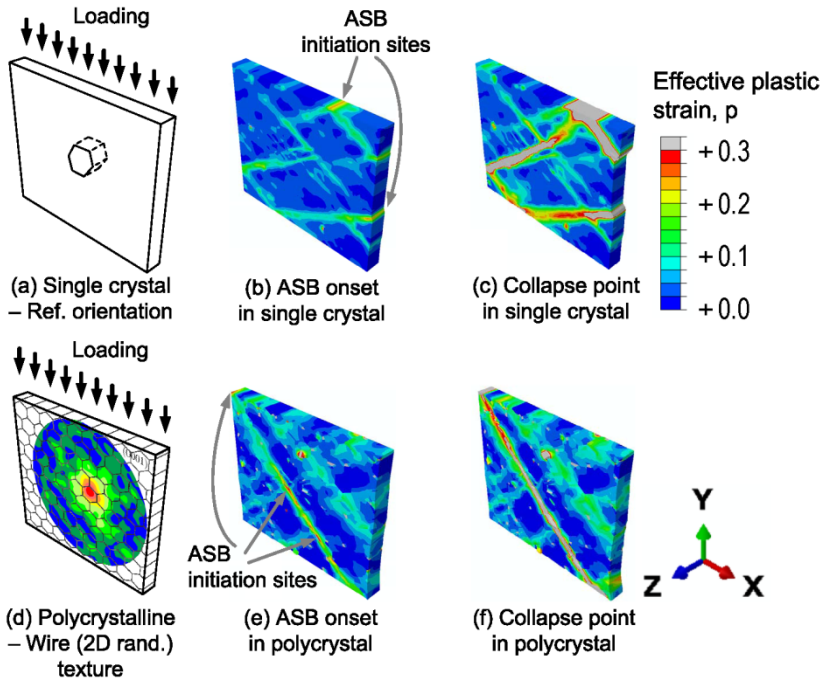

Figure 3 Shear localization in HCP single crystal and polycrystalline specimens with v_{peak} = 20 m/s; the snapshots are taken at (b) ε=4.6%; (c) ε=8.5%; (e) ε=4.5%; and (f) ε=7.2% respectively; ASB initiation sites are highlighted in (b) and (e).

In contrast, the nucleation of the ASB in the polycrystalline specimen initiates from the interior of the specimen (at the point of highest strain shown) as seen in Figure 3(e). In fact, the initiation is found to occur at the boundary of a grain well-orientated for slip. The ASB then tends to develop in grains having similar orientation, therefore giving early slip, which

then links to form the ASB. In both the single and polycrystal samples subjected to dynamic uniaxial loading, the overall direction of the ASB reflects the macroscopically imposed direction of maximum shear stress. However, the role of local crystal anisotropy is also reflected in that the width of the shear band is observed to be larger in the single crystal than that in the polycrystal. This is why the local heat generation is significantly greater in the narrower shear band in the polycrystal resulting in the very differing temperatures achieved in each. For instance, at a macroscale strain of 7%, the maximum local temperature in the polycrystal ASB is 533°C compared to 413°C in the single crystal ASB. In the polycrystal, several grains are oriented such that prism slip aligns with the macroscopically imposed maximum shear, favouring early slip nucleation and stronger localisation than that in the single crystal, for which the prism planes are inclined at 15^{o} to the maximum shear, thus inhibiting slip relative to the polycrystal, and leading to a wider slip band. A further consequence is that both initiation of ASB formation, and sample collapse are reached earlier in the straining history in the polycrystal compared to the single crystal. This signals the potentially significant role of texture in both advantaging and inhibiting ASB formation and development in polycrystal deformation, and is addressed in detail later in the paper.

Figure 4 shows the corresponding macro-level stress – strain responses for the two cases, where the differences in the collapse strains may be seen. In addition, it is observed that the single crystal behaviour shows considerably more oscillation and for longer during loading than the polycrystal. Naturally, the polycrystal with random texture provides an order higher potential for wave scatter thus giving a much more smooth, averaged, behaviour in the stress response compared with the single crystal. The figure also shows the average uniaxial stress is higher for the polycrystal than for the single crystal under the same dynamic loading. This results from polycrystal grain orientations, several of which may be incompatible with easy

slip (for example, c+a slip strength is approximately three times that of a-type slip), thus increasing the effective yield stress.

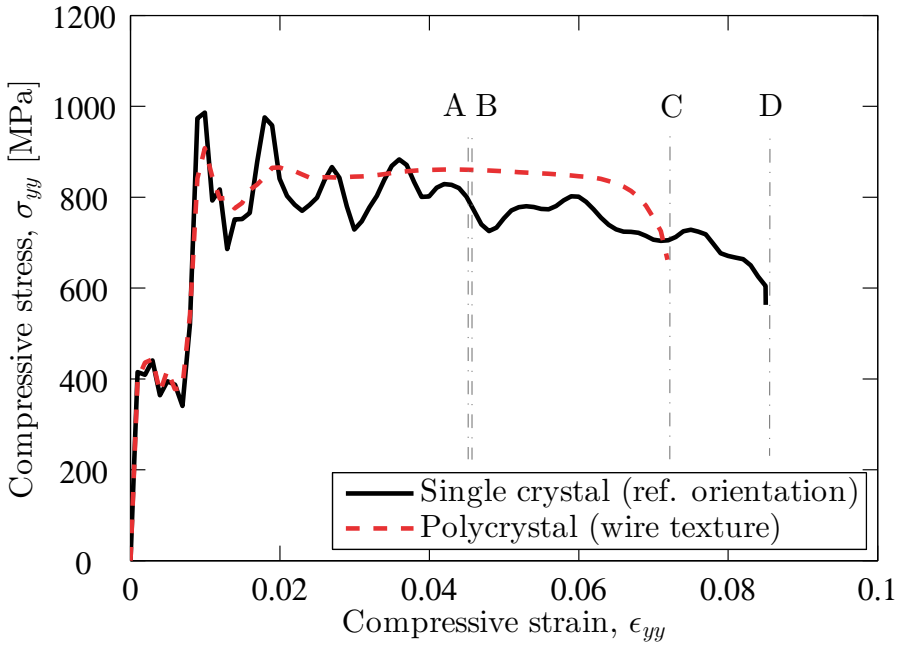

Figure 4 Macro-scale dynamic (v_{peak}=20 m/s) stress-strain response for single and polycrystal models under compression; "A" and "B" represent the ASB onset points for polycrystal and single crystal models respectively; "C" and "D" are separately the failure points in the polycrystal and single crystal models.

3.3 Loading velocity (strain rate) effects in ASB formation

Many engineering alloys, particularly for high homologous (T/T_m) temperatures, show rate sensitivity effects, and a characteristic of the near-alpha titanium alloys is that their rate sensitivity is high even at low homologous temperatures (eg at 20^{o}C). In high rate loading of polycrystals, dynamic or inertia effects exist, leading to significant inhomogeneity of stress resulting, for example, from the propagation of stress waves. This generates a spatial distribution of strain rates, so that the rate sensitivity of the material leads to an additional spatial variation of stress response to differing strain rate, which potentially impacts upon the overall polycrystal response. In addition, increasing strain rate leads to greater internal heat

generation for a given strain occurring over progressively shorter times. A consequence is that the time available for thermal conduction decreases with increasing strain rate, thus potentially leading to much higher local temperatures, and the likelihood of much more local softening and consequent severe strain localisation. To investigate the role of strain rate in polycrystal ASB formation, a broad range of loading rate is applied (for given rise time) resulting in responses from quasi-static ($v_{peak}=2\times10^{-6}$ m/s) through to those giving rise to strong dynamic (ie wave or inertia-dependent) (v_{peak}=20 m/s) responses. The corresponding strain rates, given the polycrystal sample dimensions considered in this work, then vary from 1×10^{-2} to 1×10^{5} s^{-1}. A rise time of 0.001μs is considered for this study as it is known to introduce dynamic effects in the present specimen dimensions for the higher target velocities. The targeted total applied deformation in this study is a compressive strain of 10%.

Figure 5 shows the spatial distribution of effective plastic strain resulting for the same polycrystal subjected to two extremes of applied velocity, namely that leading to quasi-static behaviour, and that resulting in a strongly dynamic response. It is seen from Figure 5(a) for the quasi-static loading that some localisation of plasticity occurs, but that it remains rather diffuse relative to the high-rate loading shown in Figure 5(b) in which a strong ASB is seen to have formed. The quasi-static loading leads to the establishment of two wide shear zones at 45° to the loading direction. Strong shear localization is not developed. The significant differences observed for the two loading rates result directly from the balance between the rate of thermal diffusion and the rate of plastic dissipation. For the high-rate loading, the dissipation rate is high relative to the rate of conduction, so that temperatures are much higher, softening occurs and reinforces further slip development and internal heat generation. The consequence is the formation of an ASB. At the low loading rate, however, the dissipation rate is lower such that thermal conduction redistributes temperature gradients, thus inhibiting the strong softening and strain localisation, resulting in a much more diffuse distribution of

shear banding, and the absence of an ASB. It is informative to examine particularly the resulting temperature distribution along the ASB in the high-rate case, and along the corresponding more diffuse zone of shear in the low-rate example. These temperature distributions along path AA', shown in Figure 5(b), at an applied strain of 10% for the two loading rates are shown in Figure 6.

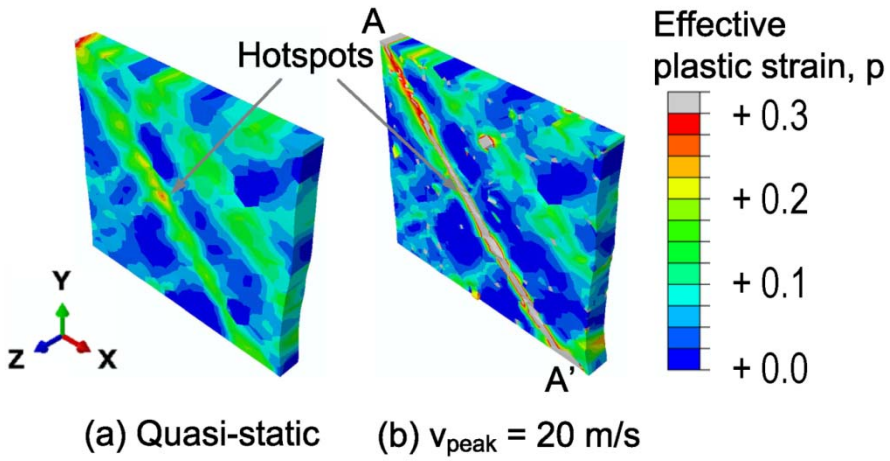

Figure 5 Compression of polycrystalline specimen up to 7% with (a) quasi-static loading and (b) dynamic loading with v_{peak} = 20 m/s

Firstly, the much higher temperature achieved for the high-rate loading is noted, but so is the much more heterogeneous nature of its distribution, indicating a really strong influence from the polycrystal micro-texture, resulting from crystallographic orientation changes from one grain to the next along path AA'. The low-rate result is conspicuous in the absence of strong variation, indicating that provided sufficient time is available over the loading, thermal diffusion tends to equalise the temperature distribution, but at the high rate, strong differences from grain to grain in internal heat generation exist (resulting from micro-texture variations), leading to highly localised flow in grains well-orientated for slip, pushing up local temperatures and reinforcing localisation and progression of slip. This is evident in the resulting distribution of slip along path AA' within the ASB shown in Figure 5(b). This result

provides further evidence that micro-texture, and potentially texture, are important in influencing ASB formation, and conversely, that careful control of texture may provide methodologies for control of adiabatic shear banding. It also suggests that there may exist combinations of grain orientations, or contrived micro-textures, which provide stronger resistance to ASB formation. This possibility is addressed further in a later section on texture effects.

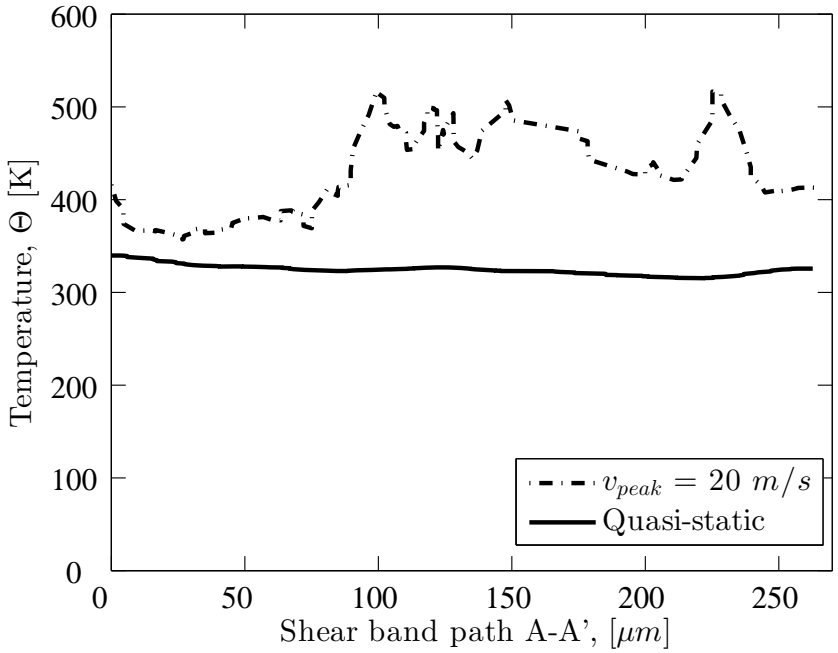

Figure 6 Temperature profile along the shear band path A-A' defined in Figure 5 (b)

3.4 Rise time, strain rate and inertial effects

It is expected that variation in loading rise time influences shear localization (Wright and Ockendon, 1996; Zener and Hollomon, 1944). This has also been reported by many including Bonnet-Lebouvier and Klepaczko (2002). A shorter rise time leads to both higher strain rates, and stronger inertia (stress wave) effects, and reduces the time scales available for thermal diffusion; higher stress levels and stronger localisation are anticipated. It is therefore expected that the selection of rise time for a fixed target loading velocity also

influences material response, since it influences both the rate of change of strain rate, and the inertial (stress wave) behaviour.

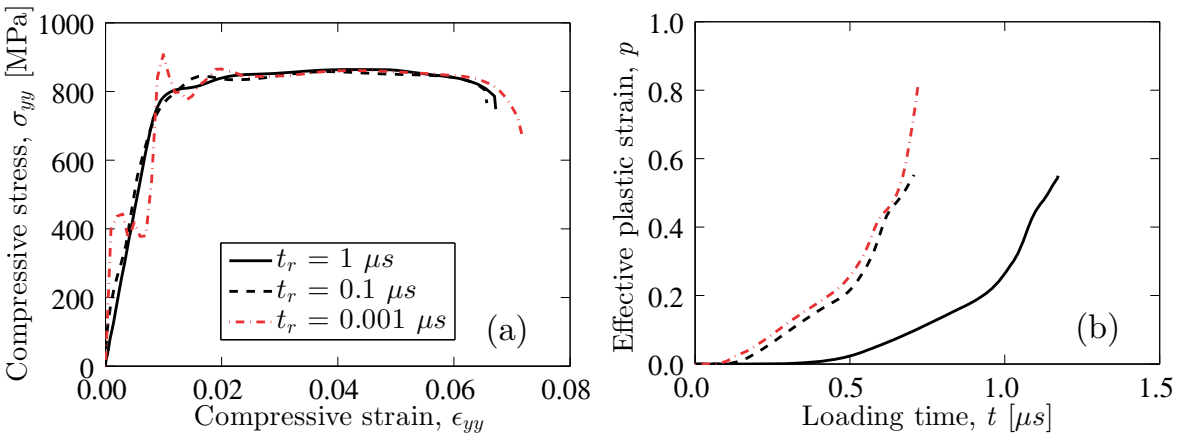

Figure 7 Rise time effect (v_{peak} = 20 m/s) in: (a) macroscale stress-strain response; (b) Effective plastic strain history at typical hotspot within the shear band

In order to investigate this behaviour at the microstructural level within our crystal plasticity approach, we examine polycrystal response with a fixed peak velocity of 20 m/s, a targeted applied deformation of 10% compressive strain, but consider a range of rise times. The results are shown in Figure 7, in which rise times of 1.0, 0.1 and 0.001 μs are imposed. The resulting average, macro-level stress responses are shown in Figure 7(a) for the three rise times. The result for the shortest rise time shows the strongest dynamic effects, but the average responses are not seen to vary significantly. However, Figure 7(b) shows a marked change in the strain accumulation at a chosen 'hotspot' (identified in Figure 5(b)) within the developing shear band. For a given loading time (or equivalently, applied strain), a decreasing rise time tends to increase the hotspot strain accumulation, thus concentrating the strain localisation as reported elsewhere. The mechanistic basis for this is as discussed above in Section 3.3 in which the rate of straining, thermal diffusion, and temperature increase enhancing softening, considered at the micro-texture, all couple to lead to ASB formation. As

rise time increases, so the strain rate drops, inertial effects diminish, temperature uniformity becomes greater, and the potential for ASB formation decreases, approaching the response anticipated under quasi-static conditions.

3.5 Thermal softening

While the consequences of thermal softening have been implicitly considered in the previous sections, because it is argued to play such a profound role at the micro-texture length scale for ASB formation, the phenomenon is addressed separately and in more detail in this sub-section. To measure the temperature variation in the formation of adiabatic shear banding remains an experimental challenge; its accurate measurement requires a spatial resolution of about 10 μm, and temporal resolution of about 10 μs. Within such fine resolutions in space and time, it is necessary to capture a potential temperature rise of order ~1000 K. In the present work, we utilise the thermal crystal plasticity model in order to investigate internal heat generation from plastic dissipation, and the resulting temperature transients which arise in association with ASB formation. The textured polycrystal sample is subjected to the velocity loading and unloading history shown in Figure 8; the unloading and subsequent load-free periods are included in order to track the thermal transients once the ASB has formed. A target velocity of 20 m/s with a rise time of 0.001 μm is considered which generates dynamic wave propagation and internal temperature rise. After 0.7005 μs, the total deformation applied is 7%. The unloading velocity has the same rate, and once zero velocity has been achieved, the thermal analysis continues for a further 7.0 μs.

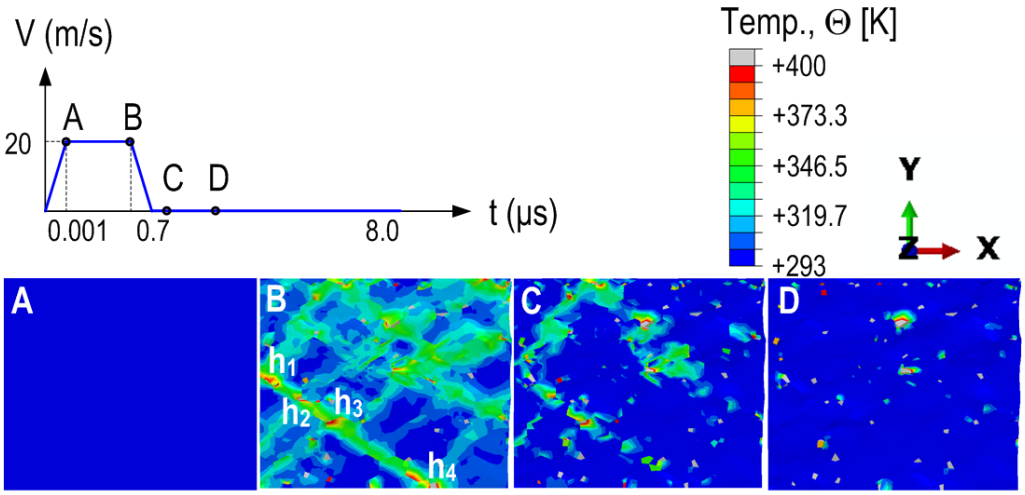

Figure 8 Temperature variation during load and unload in the textured specimen. The snapshots of temperature distribution are taken at t_A=0.00144μs, t_B=0.69μs, t_C = 0.77μs, and t_D=0.926μs corresponding to points A, B, C and D shown in the figure. Point D corresponds to the time at which the local temperature has effectively diminished to 293 K.

As indicated in Figure 8, four spatial temperature distributions at points A, B, C, and D in the loading history are extracted, and shown. It can be seen from the spatial distributions that the temperature remains less than 400 K at time point A which occurs at an applied strain of 0.005%. Indeed, very little change in the uniform temperature of 293 K has yet taken place. The major shear localization, at least as indicated by the temperature distribution, appears fully formed at point B and the main ASB aligns at about 60° with respect to the loading direction. In this polycrystal, the texture chosen is such that the predominant c-axis direction lies at ~30° to the loading direction such that the ASB is largely prism slip which localises because of the thermally-induced softening. During unloading between points B and C, it can be seen that significant conduction has taken place to generate a much more uniform temperature distribution, and by point D after a further ~0.16 μs, the temperature has largely returned to a uniform distribution of 293 K. The cooling rate within the shear band in this example is found to be about 340 K/μs. Very high transient cooling of adiabatic shear bands

has been reported by Peirs et al. (2010), though in their study, the authors didn't quantify the magnitude of the ASB cooling rate.

Interestingly, a heterogeneous temperature distribution is seen within the shear band. Four hotspots within the ASB develop at points labelled h_1, h_2, h_3 and h_4, as indicated in Figure 8. The representative plastic strain rates at these points are correspondingly 0.88, 1.13, 1.1, and 0.84 μs^{-1}, and are the greatest in the complete polycrystal domain. Clifton et al. (1984) also found that heat generation is greatest in the regions of highest strain rate. It has also been found experimentally that hotspots may occur at multiple locations within a shear band, and use of high speed infrared cameras (Guduru et al., 2001a; Guduru et al., 2001b) and by pyrometry (Ranc et al., 2008) confirm this.

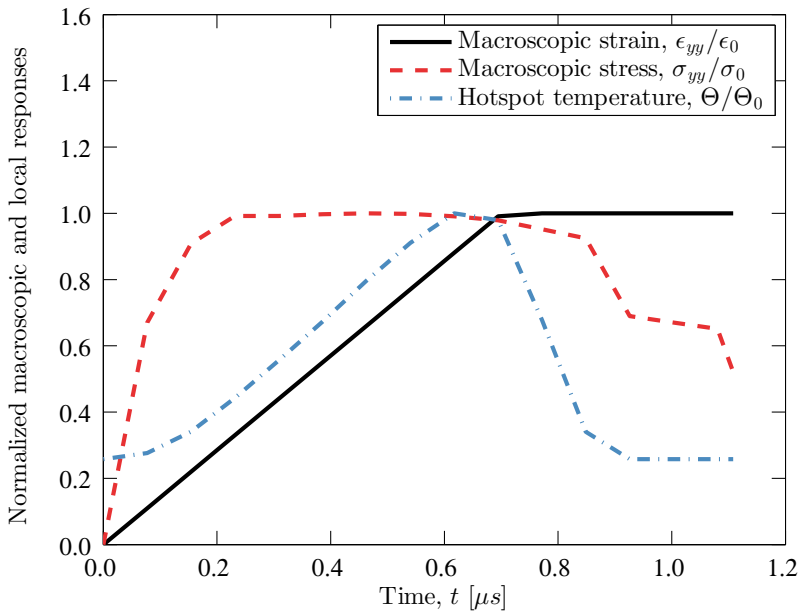

Figure 9 Macroscopic stress, strain and *local hotspot h_2* temperature history. Quantities shown are normalised by ε_0 = 7%, σ_0=855 MPa and Θ_0=350 K

Figure 9 shows the variation with time (loading history) of macro-level polycrystal stress and strain in the loading direction, together with the local hotspot h_2 (identified in Figure 8) temperature variation. All quantities are normalised as detailed in the figure. The model

specimen shows (stress) softening when the local hotspot temperature reaches ~350 K at 0.62 μs. The global load drop depends on the rival effects of thermal softening due to temperature rise, strain rate hardening by thermally activated dislocation and slip, and hardening associated with increased applied strain. From the velocity unloading to zero at 0.7015 μs, the internal heat begins to disperse resulting in the progressive redistribution of temperature. The ASB cooling, and temperature redistribution process is found to occur within ~0.23 μs, giving rise to much faster cooling than the heating under this loading history.

3.6 Texture effects in ASB formation

Recent studies indicate that specimen dimensions and corner radii influence the initiation of ASBs, and the reproducibility of the high strain rate impact performance of hat-shaped and Hopkinson bar samples is in fact found to be low (Peirs et al., 2010). This could be attributed to the above, but another potentially important factor is here argued to be the underlying metal texture, and micro-texture, both of which have already been shown to be of importance in influencing ASB formation. Hence, in this section, we consider in some detail the effects of representative HCP textures and their role in failure mode and onset of ASB formation under both uniaxial compression and simple shear dynamic loading. Figure 10 shows the range of orientation distribution function representations of HCP textures considered in the study.

The texture (a), termed RD split, is often seen in HCP metals with c/a ratio larger than 1.633 such as for Zn and Zr (Tenckhoff, 2005). TD split in Texture (b) is often seen in processed Ti polycrystals for which the c/a ratio is smaller than 1.633. Texture (c) is simply Texture (b) rotated through -90^{o} about both the z and x-axes, such that many crystal c-axes then lie in the applied loading direction for dynamic compression. Texture (d) is close to, but not strictly, uniform random, since the minimum and maximum intensity values are 0.03 and

3.5. Texture (e) is generated to give an in-plane random crystal orientation with the crystal c-axes close to parallel to the z axis for most grains. Finally, Texture (f) represents uniform-random texture in three dimensions such that the minimum and maximum intensity values are close to unity.

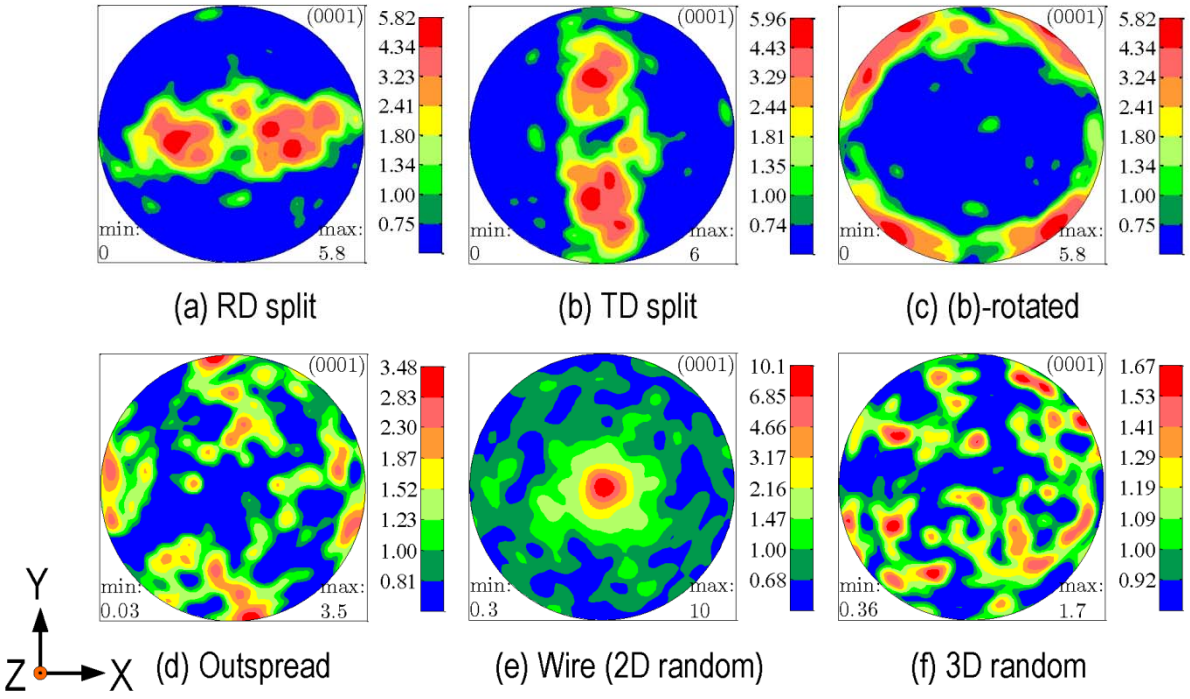

Figure 10 Range of HCP polycrystal textures studied

For the six textures shown in Figure 10, textures (a), (b) and (d) are obtained from material characterisation methods (eg EBSD or XRD) while the remaining three are established numerically. As shown in Table 1, Kearns factors are calculated for the textures shown in Figure 10. Kearns factors are commonly utilised in technological applications because of their simplicity, hence their consideration here, and further information is provided in Appendix B. The three factors for a given texture represent the fraction of HCP polycrystal basal poles that are orientated along the three orthogonal axes. The sum of the three factors therefore gives a value of unity. It is reasonable to find that f_3 is larger than the other two components in textures (a), (b) and (e) since most of the crystal basal poles (the c-axes) align

closely to the z-axis. The rotation of Texture (a) into Texture (c) results in most basal poles being in-plane, leading to a reduced f_3 in Texture (c) as compared to Textures (a) and (b). Due to the uniform random distributions of crystal orientations for in-plane and 3D textures (e) and (f) respectively, f_1 and f_2 are very close in Texture (e) while the three Kearns factors are almost identical in Texture (f).

Table 1 Kearn's factors in six textures

Textures	Factor components		
	f_1 - (x)	f_2 - (y)	f_3 - (z)
(a): RD split	0.34	0.13	0.52
(b): TD split	0.13	0.39	0.48
(c): (b)-rotated	0.39	0.48	0.13
(d): Outspread	0.35	0.37	0.28
(e): Wire (2D random)	0.26	0.26	0.48
(f): 3D random	0.34	0.33	0.32

With loading and boundary conditions introduced above and given in Figure 2 for dynamic uniaxial compression and shear, respectively, the average, macro-level stress and strain behaviours for the six textures are given in Figure 11 for a loading velocity of 20 m/s with a rise time of 0.001 μs. The model specimens are loaded towards 10% straining in compression and shear directions, respectively. It is seen from Figure 11(a) that Textures (c), (d), and (e) lead to strain localisation and sample failure at about 7% under uniaxial dynamic compression loading. However, in Figure 11(b), Textures (b), (c), and (f) fail due to localisation at about 5.5% under dynamic shear loading.

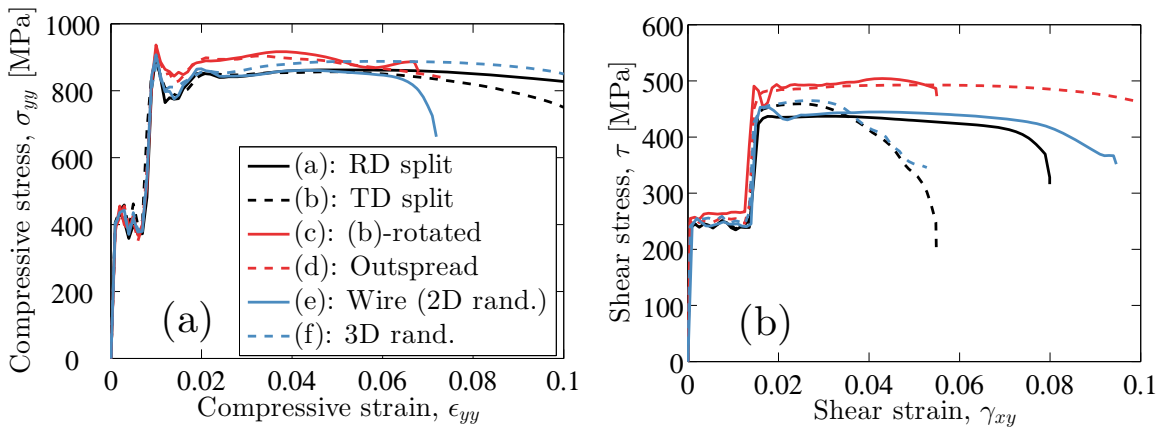

Figure 11 Macro-level stress versus strain response under (a) dynamic compression and (b) dynamic shear (v=20m/s) for textures (a) to (f).

The localised plasticity and ASB formation are shown for uniaxial loading in Figure 12 and for shear loading in Figure 13 respectively. Particularly, ASB formation for textures (c), (d) and (e) are apparent in Figure 12(c), (d), and (e) for dynamic compression to ~7% strain and has developed to the extent that overall softening occurs, leading to material failure. The other textures ((a), (b) and (f)) under dynamic uniaxial loading also show ASB formation, but at a later strain of 10%, for which significant overall (macro-scale) softening (and therefore failure) has not yet definitively taken place.

As shown in Figure 12, model specimens with RD split and TD split textures ((a) and (b)) develop similar shear banding typically orientated at about 45° to the loading (y-) direction. The crystal c-axes are orientated to the global z-axis at about 30°, separated in to either RD/x or TD/y axis orientations and prism slip directions lie at about 30° or 60° to the loading direction, indicating prismatic slip predominantly contributes to shear banding. The TD split texture (b) leads to the development of shear banding across the polycrystal sample, but this pattern appears to be inhibited by another weaker 60° shear band developing in the RD split (a) textured specimen. When rotating texture (a) and aligning its c-axes towards the loading direction as in texture (c), this increases the material strength in terms of flow stress (see Figure 11). However, the shear banding in Texture (c) is less diffuse in comparison with

those in Figure 12(a) and 12(b), reflecting the inhibition of a-type slip. The shear band in this case is orientated at about 60°， although this has been blocked by an apparent band of strain localisation at about 85°. Recall that texture (c) fails at a strain level of ~7% whereas neither texture (a) nor (b) has failed even at 10%, indicating stronger localisation in texture (c). Figure 12(g) shows independent experimental observations by Peirs et al. (2013) of similar ASB orientation to that in Figure 12(a) and (b) for similar texture. Figure 12(h) also from experiments by Peirs et al. (2013) shows ASB formation for a texture similar to that in (c), also showing good agreement in ASB orientation with respect to loading. Returning to Figure 12(a) and (b), the distinctive "V" shaped strain banding visible is also observed in the Peirs et al. (2013) experiment, shown in Figure 12(g).

In Figure 12 (d), (e) and (f) for near random, in-plane random and 3D random textures respectively, all give rise to strain localisation at about 45^{o} to the loading direction, but it is notable that texture (f) shows considerably more diffuse straining compared to both (d) and (e) , both of which result in ASB formation and failure at a strain of 7% compared to texture (f) which has not failed at a strain of 10%. Texture (d) shows an interesting apparent deviation in the course of the ASB formation, likely relating to local micro-texture features. We return to this in some detail in the next section where we examine the high-rate shear response to texture.

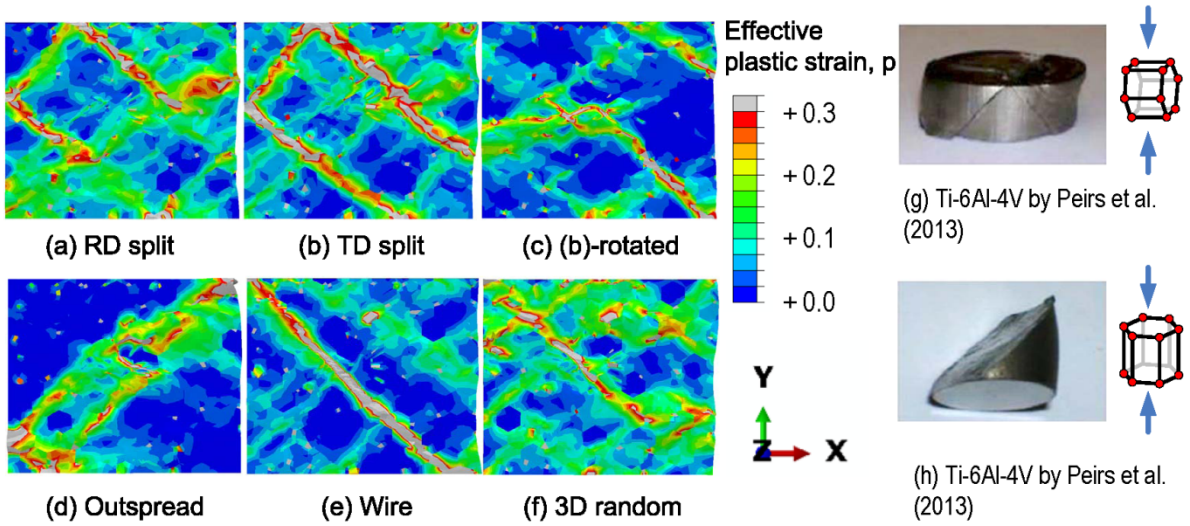

Figure 12 Failure modes for six textures under dynamic compression (v_{peak}=20m/s). The failure strains ε_{yy} at which the analyses terminate are: (a) 10%; (b) 10%; (c) 7.0%; (d) 7.4%; (e) 7.2% and (f) 10%. Experimental failure modes for dynamic compression are: (g) prismatic slip localisation in Ti-6Al-4V by Peirs et al. (2013), and (h) loading along c-axis in Ti-6Al-4V by Peirs et al. (2013) generating failure parallel to c+a planes.

Figure 13 shows the numerical results obtained for simple shear loading, in which results for textures (b), (c) and (f) show the formation of ASBs and failure for low strain levels (about 5.5%), whereas for the other textures (a), (d) and (e), ASBs are also developed as shown in Figure 13, but the strain levels for which this occurs are much higher (8, 10 and 9.5% respectively) as seen Figure 11(b). When dynamic shear loading in terms of velocity is applied at the top of the model specimen (shown in Figure 2(d)), shear bands develop in all the considered textures parallel to the shear loading direction. This failure mode is seen in Hopkinson bar tests on alpha-Ti (Meyers et al., 1994) and Ti-6Al-4V (Peirs et al., 2010), and these independent experimental results are shown in Figure 13(g) and (h) respectively. Note that shear loading as experienced in testing of top-hat specimens is often associated with large, non-uniform compressive stress while the shear bands developed in the six textures in Figure 13 are under dynamic simple shear loading. However, the similar ASB formed in the numerical and experimental tests could indicate that shear deformation governs the overall

response in the local shear zone in the top-hat shear experiments. It is possible for several parallel shear bands to develop in the samples as demonstrated by the RD split (Figure 13 (a)) and TD split (Figure 13 (b)) textures for which prismatic slip is favoured. As before, with more diffuse slip, when more shear bands develop, the total deformation is less focused on a single ASB and the corresponding failure strain is high. For example, Texture (d) leads to failure but at a higher shear strain of 10% and the plastic strain is much more distributed than that in other textures. In this texture, it is seen that the strongest shear band is blocked by one grain which is badly orientated for slip.

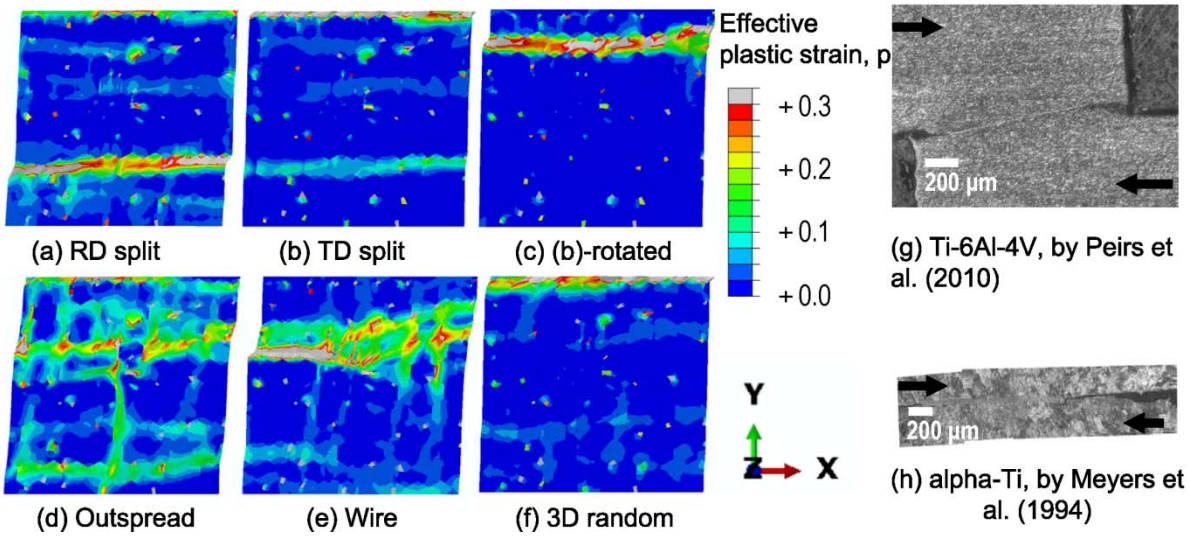

Figure 13 ASB formation for six textures under dynamic shear (v_{peak}=20m/s). The applied strains γ at which failure occurs are: (a) 8%; (b) 5.5%; (c) 5.6%; (d) 10%; (e) 9.5% and (f) 5.3%.

In order to investigate further the observed micro-texture effects, Path B-B' in Figure 14(a) has been introduced for Texture (d). The grain orientations along Path B-B' are shown schematically in Figure 14(c) in which the particular grain badly orientated for slip with respect to shear loading is highlighted in red. This results in the low strain accumulation visible in this grain in Figure 14(a), apparently blocking the ASB formation. We investigate this further by pro-actively altering the orientation of the hard grain to make it well-orientated

for slip, as indicated in red in Figure 14(d), with a prismatic plane parallel to the shear direction. The high-rate shear analysis is repeated and the new result obtained is shown in Figure 14(b), for which a much more significant single shear band has developed compared to that in Figure 14(a). In addition, the failure strain has been reduced from 10% to 7.2%. This demonstrates that micro-texture may be potentially contrived in order to inhibit or prevent the onset of ASB formation, thus delivering tailored alloys resistant to shear band failure in impact. Sun et al. (2014) have reported that shear banding favours crystals well-orientated for prismatic <a> slip. The current work supports this assertion and goes further to make clear that the inclusion of a single badly oriented grain (for slip) along the shear band path has the potential to increase straining for which ASB occurs by significant margins.

The polycrystal macroscale stress strain behaviour for the original and modified orientation combinations is shown in Figure 14(e). Modifying the grain orientation to encourage continuity of slip is interestingly seen to increase the flow stress but clearly encourage localisation and early ASB failure. The increase in flow stress may be attributed to the strain rate sensitivity of Ti-6Al alloy because of the considerably higher strain rates and strain localisation for polycrystal (b). The average temperature rise in this case is about 190°C and the maximum local shear band temperature rise 427 °C, giving strong strain rate sensitivity.

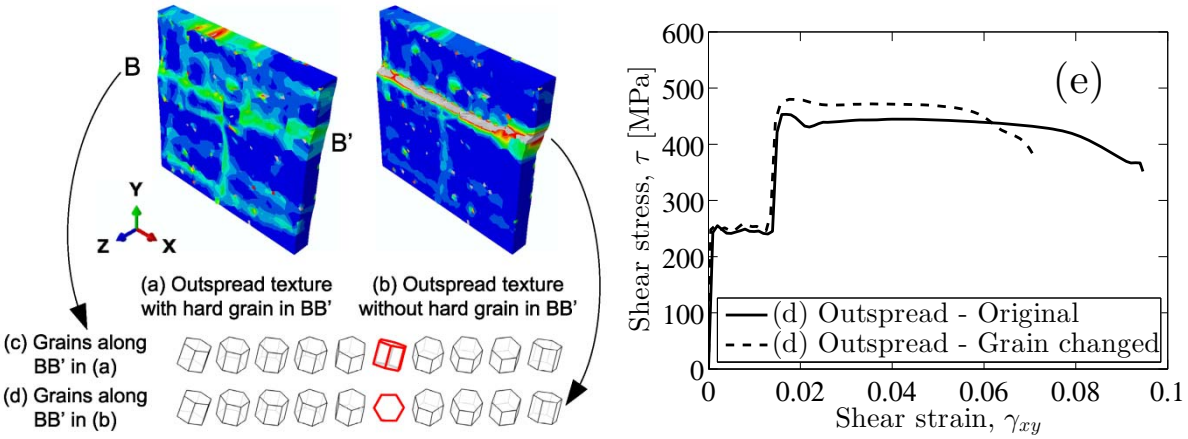

Figure 14 Effective plastic strain fields (a) and (b) obtained for the ASB path crystal orientations (Path B-B') shown in (c) and (d) respectively, and (e) the resulting macro-level stress strain response showing the failure strains 10% and 7.2% for (a) and (b), respectively.

3.6.1 High-rate strength dependence on texture

In passing, we examine the effect of texture on high-rate strengths, which are extracted from Figure 11 for the dynamic uniaxial compression and shear tests and are shown in Figure 15 as a function of the Kearns factor associated with the relevant loading direction. That is, for dynamic compression, the y-direction Kearns factor (f_2) is chosen, whereas for the dynamic shear loading, the x-direction (f_1) factor is chosen. The strength is taken to be the average flow stress obtained after dynamical oscillatory behaviour has diminished but before macro-scale softening commences. Hence, in the case of compression, the strength is taken to be average flow stress over strain range from 0.025 to 0.056, and for shear, over the shear strain range from 0.023 to 0.03. A small increase in strength is observed with increasing Kearns factor component since this reflects the increasing slip strength contribution associated with the higher fraction of crystal c-axes orientated with the loading direction.

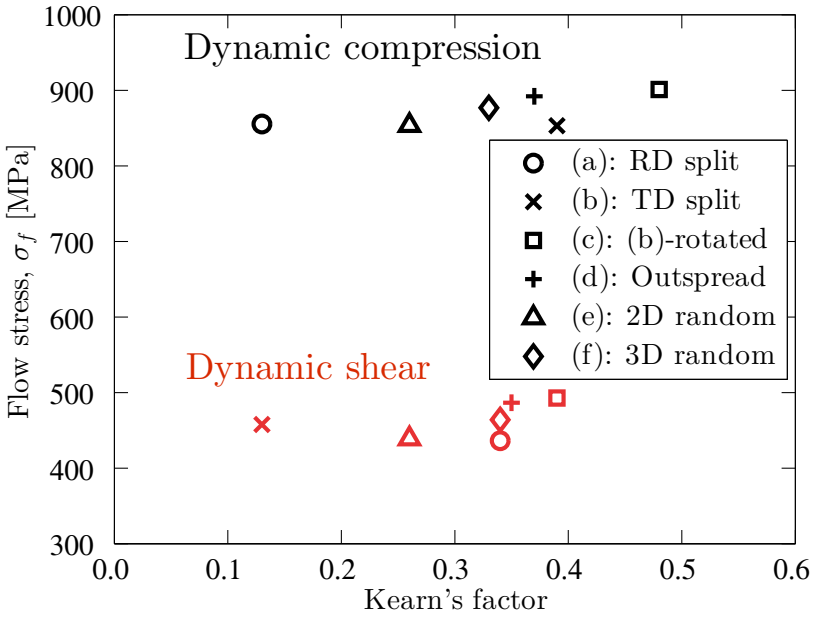

Figure 15 High-rate strength with respect to Kearns factor for the range of textures shown in Figure 16

3.6.2 Texture-dependence of ASB formation

In this final section, we aim to summarise the role of texture on the initiation and formation of ASBs, particularly with respect to the strain level required for initiation. The latter measure, while not providing a definitive quantification of ASB formation, is at least important technologically and industrially, but there has been much research aimed at establishing an appropriate quantitative measure. We note that Hill (1962) presented a general theory of bifurcation of a homogeneous elastic-plastic flow field into a localized band. Asaro and Rice (1977) extended Hill's idea and showed that it was possible to generate shear banding in weak work hardened materials rather than materials experiencing strain softening. The onset of shear banding was found to be due to the deviation of the normality of the flow rule, which was caused by non-Schmid effects at the onset of cross slip. Asaro and Rice (1977) addressed strain localization quantitatively through linking the micromechanical slip to macroscopic plastic consistency conditions. Their quantitative

measure has been specified as a critical plastic hardening rate at the inception of localization, through examples of initially-homogeneous rate insensitive single crystals. The specific form of this quantitative measure of localization was given for a constitutive model that allowed for non-Schmid effects in cross-slip. Based on a dislocation model of the process, the quantitative measure for ASB onset was developed. Antolovich and Armstrong (2014) also address quantitative onset of ASB formation. Considère's criterion (Considère, 1885), derived from the inflection point condition, is one of the well-known macroscopic onset measures of necking. This criterion has been extended for rate sensitive materials by consideration of a rate sensitivity index (Hart, 1967; Jia et al., 2001). Staker (1981) found experimentally that the onset of ASB in AISI 4340 steel could be represented by a true shear strain based criteria. It is interesting to note that an upper bound based on conventional Considère's criterion and a lower bound by Staker's equation (Antolovich and Armstrong, 2014) may be established. The data scatter between the upper and lower bounds was attributed to sources of geometric instability and microstructural texture, which is independent of any thermal softening mechanism (Walley, 2007). However, in the present work, we address the onset of ASB formation with full consideration of internal heat generation, the resulting heat transfer, and local thermally-driven strain softening in the rate-sensitive crystal model. In particular, we address the roles of texture and micro-texture in ASB formation, but in order to do this quantitatively, it remains necessary to introduce an appropriate quantitative measure of shear band formation. In light of the discussion above, we therefore choose the technologically-relevant (and industrially preferred) point of instability occurring with respect to the macro-scale stress – strain response resulting from the analysis of the aggregate of grains considered in our textured, and micro-textured model polycrystals.

As has already been shown, ASB formation also depends very strongly on rise time and velocity, but for the purposes of brevity and clarity, we address just one set of given velocity conditions for which texture is then varied. However, to begin, consider loading all the model specimens to 7% total deformation both by dynamic loading (v_{peak}=20m/s) and with quasi-static loading with strain rate of 10^{-2} s^{-1}. The shear localization resulting at a strain level of 7% is illustrated in Figure 16 for the range of textures considered, here shown by the effective plastic strain. This quantity clearly shows the establishment of very much more significant localisation and inhomogeneity for all textures for the dynamic loading (from (a) to (f)) compared to quasi-static ((g) to (l)). At this strain level, it is apparent that shear bands form in textures (c), (d) and (e) under dynamic loading but not so for the other textures in (a), (b), and (f). This demonstrates that ASB onset is very dependent on HCP texture.

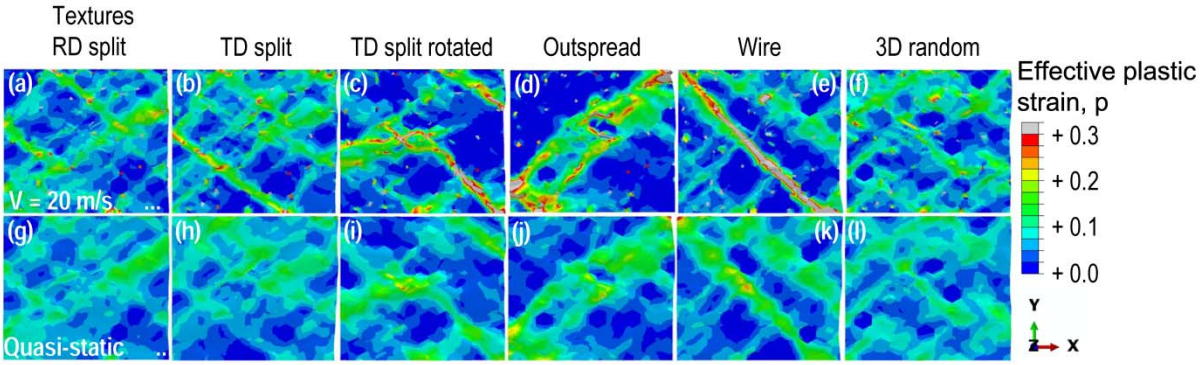

Figure 16 Shear localization for the six textures under consistent 7% compressive strain, with (a)-(f) under dynamic loading with v_{peak}=20 m/s and (g)-(l) under quasi-static loading for the same set of textures

Hence, for the specific dynamic compression loading conditions (v_{peak}= 20m/s), the range of textures have been systematically analysed in order to establish the strain level required in order to establish the onset of ASB formation. For this purpose, ASB formation is quantitatively defined by the onset of softening (i.e. $d\sigma/d\varepsilon = 0$, or $d\tau/d\gamma = 0$) shown by the corresponding macro-scale stress strain response, and a discussion of this quantification, and

the context provided by the research literature, has been given above. The summary results are shown in Figure 17 for both dynamic compression and shear loading, demonstrating strong dependence of ASB onset strain on texture. In fact, the strain required in order to initiate ASB formation is found to differ by up about 0.03 (3%) within both the compression and shear loading regimes for the textures considered. It therefore becomes clear that a 'critical strain' for the onset of ASB formation is not universal since it depends so much on texture and, as was shown earlier, on micro-texture. The ASB onset strain is generally found to be higher for dynamic compression than that for dynamic shear, since ASB formation under dynamic shear is near-parallel to the shear loading direction. Under dynamic compression, the shear band orientation depends on texture but has been found to be between 30° and 60° to the loading direction, and often occurs along with a more complex shear band network, resulting in much longer effective lengths in sheared material to accommodate the deformation, thus requiring higher applied strains. One significant exceptional case is that for texture (d) where the onset strain in shear is larger than that in compression. However, referring back to Figure 13(d), it is observed that even for conditions of shear loading, a complex shear band structure has been developed, largely because of the effect of micro-texture (see Figure 14). Conversely, for compression loading in the same texture, a reasonably well-defined 45° shear band is formed, as shown in Figure 12(d). It is also interesting to find that the shear band onset strain is around 4.5% on average (based on six considered textures) and this is much higher than the 3.7% that occurs under shear loading. This indicates that with the same texture, dynamic shear loading is likely more destructive than dynamic compression.

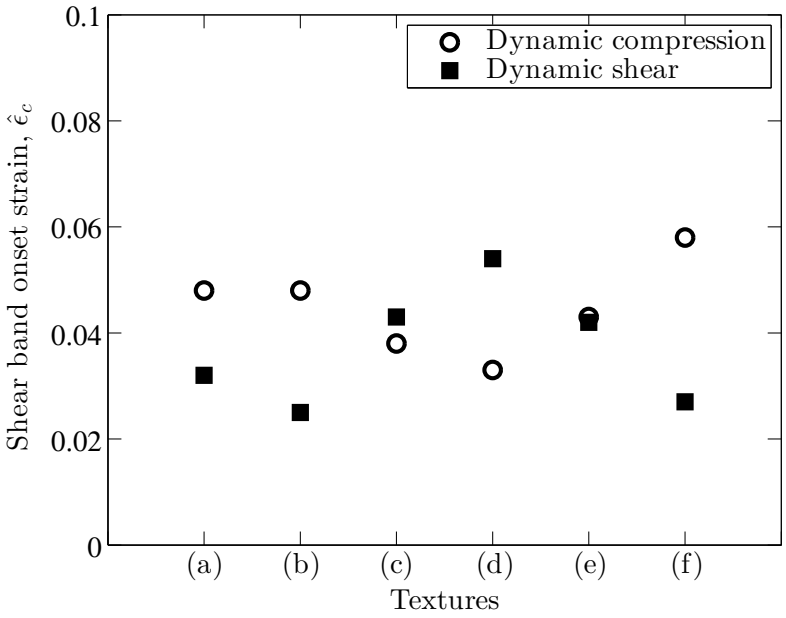

Figure 17 Adiabatic shear band onset strain for six textures under dynamic loading (v_{peak}=20m/s)

4. Discussion of caveats

Some researchers indicate that β in Eq. (4) is strain and strain rate dependent (Rittel, 2009), and taking β as a constant (eg 0.9 or 1.0) over the range of applied strains would likely result in the overestimation of temperature rise (Rosakis et al., 2000). It remains an important experimental challenge to quantify the proportion of plastic dissipation emerging as heat, and the mechanistic basis for its occurrence. In this study, however, in the absence of quantitative and empirical detail, we simplify the problem and take β to be 0.9. This is also recommended by Wright (2002).

It is the case that wave propagation is potentially affected by the model boundaries and imposed boundary conditions, and a consequence is that the failure mode captured in small-scale model samples is not fully representative of that in bulk materials. Nevertheless, within this context, it has been possible to carry out systematic studies on the nucleation of ASBs and the role of texture and micro-texture in their formation and propagation providing

considerable insight in to the importance of microstructure. The scale up of this approach to make it appropriate as a practical engineering tool therefore requires further work.

In modelling material softening phenomena (and plastic strain localisation is a classic example), there usually exist mesh dependency problems (Anand et al., 2012; Bazant and Jirasek, 2002; De Borst et al., 1993; Peerlings et al., 2001). A customary solution is to introduce length-scale dependent parameters to regularize the total potential energy to maintain the positive definiteness of the numerical problem, thereby establishing a unique solution so that the softening/weakening is reasonably represented. The regularisation is often based on a strain gradient approach, with the latter considered as an additional degree of freedom when formulating the finite element method. The problem has been mitigated in the present work through appropriate mesh refinement and consistency in mesh size local to ASB formation by virtue of the regular grain morphology adopted, and appropriate and consistent mesh refinement. However, it is recognised that such mitigation would be less effective in random morphological representations, and this necessitates the development of appropriate regularization schemes, for example through incorporation of approaches similar to those used for non-local length scale effects (Dunne et al., 2012).

5. Conclusions

The balance between the time constants associated with thermal diffusion and plastic dissipation are found to be crucial in controlling strain localisation, softening and ASB formation.

Texture in HCP polycrystals is found to have major impact on the strain required for the onset of ASB formation, with texture variation leading to differences in ASB onset strain of up to 3%. For high-rate shear, low strain to ASB formation results from TD split textures, and

high onset strain from outspread texture. For compression, random texture is shown to lead to highest ASB onset strain.

ASB development tends to occur along bands of grains with similar crystallographic orientation. Grain size affects ASB thickness, thereby affecting length scale over which internal heat generation occurs, thereby influencing local temperature. Temperature differences along forming ASBs of 150K or more are observed, influenced strongly by micro-texture. ASB cooling rates of $350K\mu s^{-1}$ or higher are observed at local ASB hotpots at which temperatures in excess of 500K are achieved.

Micro-texture has been found to play a crucial role in ASB initiation and development, and particularly in the inhibition, or disruption of ASB formation. Contrived combinations of crystallographic orientation (eg to give a classical hard-soft slip configuration) have strong influence on both the advancement and inhibition of ASB growth, leading to considerable differences in failure strain. Carefully controlled microstructures therefore provide the potential for significant technological benefits in the development of new impact-resistant alloys.

Acknowledgement

The authors gratefully acknowledge the financial support from the Engineering & Physical Science Research Council (EP/K034332) through HexMat programme. ZZ expresses gratitude to Drs Bo Lan and Ben Britton, and to Mr Barzdajn Bartosz for helpful discussion on texture in hexagonal materials. DE acknowledges AWE for their continued support of the Institute of Shock Physics.

Appendix A – Properties and Parameters

Table A.1 High-purity polycrystal alpha-Ti: temperature independent material properties

Material properties	Quantities	Reference
Thermal conductivity, k	14.99 [w/mK]	Leyens and Peters (2003)
Density, ρ	4510 [Kg/m^{-3}]	Lide (2010)
Thermal expansion coefficient	$\alpha_c = 5.6\times10^{-6}$ [K^{-1}] $\alpha_a = 9.5\times10^{-6}$ [K^{-1}]	Ho and Taylor (1998) and Pawar and Deshpande (1968)

Table A.2 High-purity polycrystal alpha-Ti: material property dependency on temperature

Temperature dependency for $\Theta \in [293,1000]$ K	
Critical resolved shear stress for basal, prismatic and pyramidal <a> slip systems $\tau_c^{b,p}(\Theta) = 0.002\times(\Theta-273)^2 - 0.3794\times(\Theta-273) + 280.45$ (A1.a) $\tau_c^{pyra}(\Theta) = 0.0011\times(\Theta-273)^2 - 1.3801\times(\Theta-273) + 867.18$ (A1.b)	Williams et al. (2002)
Young's modulus and shear modulus $E_1 = -75.329\times(\Theta-273) + 85292$ (A2.a) $G_{12} = -27.403\times(\Theta-273) + 29100$ (A2.b)	Lütjering and Williams (2007)
Specific heat capacity $C_p(\Theta) = 2.0\times10^{-7}\times(\Theta-273)^3 - 0.0003\times(\Theta-273)^2 + 0.3159\times(\Theta-273) + 519.58$ (A3)	Leyens and Peters (2003) Xue et al. (2002)

Full elastic anisotropy is adopted in this study. The constant values in room temperature are given by Dunne et al. (2007) terms of E_{11}, E_{33}, G_{12}, G_{13}, ν_{12} and ν_{13}. With temperature dependency of E_1 and G_{12} defined in Eq. (A2), one can interpolate to get the other elastic

constants. At an updated temperature Θ_{i+1}, for instance, $E_{33}^{i+1} = E_1^{i+1} \times \frac{E_{33}^i}{E_1^i}$. Using this method, one can get associated temperature dependency for G_{13} and ν_{13}. In addition, the parameters defined in the slip rule are given by Zhang et al. (2015) and they are listed in Table A.3.

Table A.3 Slip rule parameters

Material properties	Quantities	
ρ_m	5.0	[μm^{-2}]
ρ_o	0.01	[μm^{-2}]
ν	1.0×10^{11}	[Hz]
b	3.20×10^{-4}	[μm]
k	1.381×10^{-23}	[$J\,K^{-1}$]
γ_0	6×10^{-4}	
γ'	0	for single crystal
	0.05	for polycrystal
ΔH	9.913×10^{-20}	[$J\,atom^{-1}$]

Appendix B - Kearns factors

Kearns factors are used to represent the fraction of basal poles of HCP metals projected into global orthogonal axes. They serve as a simple and technologically useful index of material anisotropy and have been adopted widely in HCP metals (Anderson et al., 1999; Lan et al., 2014; Lan et al., 2015a, b). Fuller detail may be obtained from the papers by Anderson et al. (1999) and Kearns (1965). Kearns factors are given by

(C1)

$$f_1 = f_{RD} = \int_0^{\frac{\pi}{2}} \int_0^{2\pi} q(\chi,\eta) \sin^3(\chi) \cos^2(\eta) d\eta d\chi \quad \text{(C2)}$$

$$f_2 = f_{TD} = \int_0^{\frac{\pi}{2}} \int_0^{2\pi} q(\chi,\eta) \sin^3(\chi) \sin^2(\eta) d\eta d\chi \quad \text{(C3)}$$

$$f_3 = f_{ND} = \int_0^{\frac{\pi}{2}} \int_0^{2\pi} q(\chi,\eta) \sin(\chi) \cos^2(\eta) d\eta d\chi$$

where $q(\chi,\eta)$ is the normalized pole figure intensity, and it is noted that $\sum_{i=1}^{3} f_i = 1$. If the basal poles are perfectly aligned in one direction, a Kearns factor of 1.0 will be found in that direction and zero for the other two directions. For random texture, a value of 1/3 is obtained for all three directions (Kearns, 2001).

References

Anand, L., Aslan, O., Chester, S.A., 2012. A large-deformation gradient theory for elastic-plastic materials: Strain softening and regularization of shear bands. International Journal of Plasticity 30-31, 116-143.

Anderson, A.J., Thompson, R.B., Cook, C.S., 1999. Ultrasonic measurement of the Kearns texture factors in zircaloy, zirconium, and titanium. Metallurgical and Materials Transactions a-Physical Metallurgy and Materials Science 30, 1981-1988.

Antolovich, S.D., Armstrong, R.W., 2014. Plastic strain localization in metals: origins and consequences. Progress in Materials Science 59, 1-160.

Asaro, R.J., Rice, J.R., 1977. Strain localization in ductile single crystals. Journal of the Mechanics and Physics of Solids 25, 309-338.

Austin, R.A., McDowell, D.L., 2011. A dislocation-based constitutive model for viscoplastic deformation of fcc metals at very high strain rates. International Journal of Plasticity 27, 1-24.

Bai, Y., Dodd, B., 2012. Adiabatic Shear Localization: Frontiers and Advances. Elsevier, London.

Basinski, Z.S., 1957. The instability of plastic flow of metals at very low temperature. Proceedings of the Royal Society of London. Series A, Mathematical and Physical Sciences 240, 229-242.

Bazant, Z.P., Jirasek, M., 2002. Nonlocal integral formulations of plasticity and damage: Survey of progress. ASCE Journal of Engineering Mechanics 128, 1119-1149.

Bonnet-Lebouvier, A.S., Klepaczko, J.R., 2002. Numerical study of shear deformation in Ti-6Al-4V at medium and high strain rates, critical impact velocity in shear. International Journal of Impact Engineering 27, 755-769.

Chen, Y., Ghosh, S., 2012. Micromechanical analysis of strain rate-dependent deformation and failure in composite microstructures under dynamic loading conditions. International Journal of Plasticity 32-33, 218-247.

Chichili, D.R., Ramesh, K.T., Hemker, K.J., 1998. The high-strain-rate response of alpha-titanium: Experiments, deformation mechanisms and modeling. Acta Materialia 46, 1025-1043.

Chichili, D.R., Ramesh, K.T., Hemker, K.J., 2004. Adiabatic shear localization in alpha-titanium: experiments, modeling and microstructural evolution. Journal of the Mechanics and Physics of Solids 52, 1889-1909.

Childs, T., 2014. CIRP Encyclopedia of Production Engineering, in: Laperrière, L., Reinhart, G. (Eds.), Adiabatic shearing in metal machining. Springer, London, pp. 27-33.

Clayton, J.D., 2005. Dynamic plasticity and fracture in high density polycrystals: constitutive modeling and numerical simulation. Journal of the Mechanics and Physics of Solids 53, 261-301.

Clayton, J.D., 2009. Modeling effects of crystalline microstructure, energy storage mechanisms, and residual volume changes on penetration resistance of precipitate-hardened aluminum alloys. Composites Part B-Engineering 40, 443-450.

Clayton, J.D., 2010. Nonlinear Mechanics of Crystals. Springer, Dordrecht.

Clifton, R.J., Duffy, J., Hartley, K.A., Shawki, T.G., 1984. On critical conditions for shear band formation at high strain rates. Scripta Metallurgica 18, 443-448.

Coghe, F., Rabet, L., Kestens, L., 2006. Deformation mechanisms of a commercial titanium alloy Ti6Al4V as a function of strain rate and initial texture. Journal De Physique IV 134, 845-850.

Considère, A., 1885. Memoire sur l'emploi du fer et de l'acier dans les constructions. Annales des Ponts et Chaussées 9, 574-775

De Borst, R., Sluys, L.J., Mühlhaus, H.B., Pamin, J., 1993. Fundamental issues in finite element analyses of localization of deformation. Engineering Computations 10, 99-121.

Dolinski, M., Rittel, D., Dorogoy, A., 2010. Modeling adiabatic shear failure from energy considerations. Journal of the Mechanics and Physics of Solids 58, 1759-1775.

Dunne, F.P.E., Kiwanuka, R., Wilkinson, A.J., 2012. Crystal plasticity analysis of micro-deformation, lattice rotation and geometrically necessary dislocation density. Proceedings of the Royal Society a-Mathematical Physical and Engineering Sciences 468, 2509-2531.

Dunne, F.P.E., Rugg, D., Walker, A., 2007. Lengthscale-dependent, elastically anisotropic, physically-based hcp crystal plasticity: Application to cold-dwell fatigue in Ti alloys. International Journal of Plasticity 23, 1061-1083.

Field, J.E., Walley, S.M., Proud, W.G., Goldrein, H.T., Siviour, C.R., 2004. Review of experimental techniques for high rate deformation and shock studies. International Journal of Impact Engineering 30, 725-775.

Follansbee, P.S., Gray III, G.T., 1989. An analysis of the low temperature, low and high strain-rate deformation of Ti−6Al−4V. Metallurgical Transactions A-Physical Metallurgy and Materials Science 20, 863-874.

Gilat, A., Clifton, R.J., 1985. Pressure-shear waves in 6061-T6 Aluminum and alpha-titanium. Journal of the Mechanics and Physics of Solids 33, 263-284.

Gong, J., Wilkinson, A.J., 2009. Anisotropy in the plastic flow properties of single-crystal alpha titanium determined from micro-cantilever beams. Acta Materialia 57, 5693-5705.

Guduru, P.R., Ravichandran, G., Rosakis, A.J., 2001a. Observations of transient high temperature vortical microstructures in solids during adiabatic shear banding. Physical Review E 64.

Guduru, P.R., Rosakis, A.J., Ravichandran, G., 2001b. Dynamic shear bands: an investigation using high speed optical and infrared diagnostics. Mechanics of Materials 33, 371-402.

Hart, E.W., 1967. Theory of the tensile test. Acta Metallurgica 15, 351-355.

Hill, R., 1962. Acceleration waves in solids. Journal of the Mechanics and Physics of Solids 10, 1-16.

Ho, C.Y., Taylor, R.E., 1998. Thermal Expansion of Solids. ASM International, Materials Park, Ohio.

Jia, D., Wang, Y.M., Ramesh, K.T., Ma, E., Zhu, Y.T., Valiev, R.Z., 2001. Deformation behavior and plastic instabilities of ultrafine-grained titanium. Applied Physics Letters 79, 611-613.

Kearns, J.J., 1965. Thermal expansion and preferred orientation in Zircaloy. Bettis Atomic Power Laboratory, Westinghouse Electric Corporation, Pittsburgh, PA.

Kearns, J.J., 2001. On the relationship among 'f' texture factors for the principal planes of zirconium, hafnium and titanium alloys. Journal of Nuclear Materials 299, 171-174.

Khan, A.S., Suh, Y.S., Kazmi, R., 2004. Quasi-static and dynamic loading responses and constitutive modeling of titanium alloys. International Journal of Plasticity 20, 2233-2248.

Kuroda, M., Tvergaard, V., 2007. Effects of texture on shear band formation in plane strain tension/compression and bending. International Journal of Plasticity 23, 244-272.

Lan, B., Lowe, M., Dunne, F.P.E., 2014. Experimental and computational studies of ultrasound wave propagation in hexagonal close-packed polycrystals for texture detection. Acta Materialia 63, 107-122.

Lan, B., Lowe, M.J.S., Dunne, F.P.E., 2015a. A generalized spherical harmonic deconvolution to obtain texture of cubic materials from ultrasonic wave speed. Journal of the Mechanics and Physics of Solids 83, 221-242.

Lan, B., Lowe, M.J.S., Dunne, F.P.E., 2015b. A spherical harmonic approach for the determination of HCP texture from ultrasound: A solution to the inverse problem. Journal of the Mechanics and Physics of Solids 83, 179-198.

Leyens, C., Peters, M., 2003. Titanium and Titanium Alloys: Fundamentals and Applications. Wiley, Weinheim

Liao, S.C., Duffy, J., 1998. Adiabatic shear bands in a TI-6Al-4V titanium alloy. Journal of the Mechanics and Physics of Solids 46, 2201-2231.

Lide, D.R., 2010. CRC Handbook of Chemistry and Physics, 90 edition ed. CRC Press, Boca Raton, Florida.

Lindholm, U.S., 1974. Review of dynamic testing techniques and material behaviour, in: Harding, J. (Ed.), Mechanical properties at high rates of strain. Institute of Physics, London and Bristol, pp. 3-21.

Lloyd, J.T., Clayton, J.D., Austin, R.A., McDowell, D.L., 2014a. Plane wave simulation of elastic-viscoplastic single crystals. Journal of the Mechanics and Physics of Solids 69, 14-32.

Lloyd, J.T., Clayton, J.D., Becker, R., McDowell, D.L., 2014b. Simulation of shock wave propagation in single crystal and polycrystalline aluminum. International Journal of Plasticity 60, 118-144.

Lütjering, G., Williams, J.C., 2007. Titanium Springer-Verlag, Berlin Heidelberg.

Mayeur, J., McDowell, D., 2007. A three-dimensional crystal plasticity model for duplex Ti–6Al–4V. International journal of plasticity 23, 1457-1485.

Medyanik, S.N., Liu, W.K., Li, S., 2007. On criteria for dynamic adiabatic shear band propagation. Journal of the Mechanics and Physics of Solids 55, 1439-1461.

Meissonnier, F.T., Busso, E.P., O'Dowd, N.P., 2001. Finite element implementation of a generalised non-local rate-dependent crystallographic formulation for finite strains. International Journal of Plasticity 17, 601-640.

Merzer, A.M., 1982. Modelling of adiabatic shear band development from small imperfections. Journal of the Mechanics and Physics of Solids 30, 323-&.

Meyers, M.A., 1994. Dynamic Behavior of Mateirals. Wiley, New York.

Meyers, M.A., Pak, H.R., 1986. Observation of an adiabatic shear band in titanium by high-voltage transmission electron microscopy. Acta Metallurgica 34, 2493-2499.

Meyers, M.A., Subhash, G., Kad, B.K., Prasad, L., 1994. Evolution of microstructure and shear-band formation in alpha-hcp titanium. Mechanics of Materials 17, 175-193.

Pawar, R.R., Deshpande, V.T., 1968. The anisotropy of the thermal expansion of alpha-Titanium. Acta Cryst. A24, 316-316.

Peerlings, R.H.J., Geers, M.G.D., de Borst, R., Brekelmans, W.A.M., 2001. A critical comparison of nonlocal and gradient-enhanced softening continua. International Journal of Solids and Structures 38, 7723-7746.

Peirce, D., Asaro, R.J., Needleman, A., 1982. An analysis of nonuniform and localized deformation in ductile single crystals. Acta Metallurgica 30, 1087-1119.

Peirs, J., Tirry, W., Amin-Ahmadi, B., Coghe, F., Verleysen, P., Rabat, L., Schryvers, D., Degrieck, J., 2013. Microstructure of adiabatic shear bands in Ti6Al4V. Materials Characterization 75, 79-92.

Peirs, J., Verleysen, P., Degrieck, J., Coghe, F., 2010. The use of hat-shaped specimens to study the high strain rate shear behaviour of Ti-6Al-4V. International Journal of Impact Engineering 37, 703-714.

Ramesh, K.T., 2008. High Rates and Impact Experiments, in: Sharpe, W.N., Jr. (Ed.), Springer Handbook of Experimental Solid Mechanics. Springer, New York, pp. 929-960.

Ranc, N., Taravella, L., Pina, V., Herve, P., 2008. Temperature field measurement in titanium alloy during high strain rate loading - Adiabatic shear bands phenomenon. Mechanics of Materials 40, 255-270.

Rittel, D., 2009. A different viewpoint on adiabatic shear localization. Journal of Physics D-Applied Physics 42.

Rosakis, P., Rosakis, A.J., Ravichandran, G., Hodowany, J., 2000. A thermodynamic internal variable model for the partition of plastic work into heat and stored energy in metals. Journal of the Mechanics and Physics of Solids 48, 581-607.

Schoenfeld, S.E., Kad, B., 2002. Texture effects on shear response in Ti-6Al-4V plates. International Journal of Plasticity 18, 461-486.

Staker, M.R., 1981. The relation between adiabatic shear instability strain and material properties. Acta Metallurgica 29, 683-689.

Sun, J.L., Trimby, P.W., Yan, F.K., Liao, X.Z., Tao, N.R., Wang, J.T., 2014. Shear banding in commercial pure titanium deformed by dynamic compression. Acta Materialia 79, 47-58.

Taylor, G.I., Quinney, H., 1934. The latent energy remaining in a metal after cold working. Proceedings of the Royal Society A 143, 307-326.

Tenckhoff, E., 2005. Review of deformation mechanisms, texture and mechanical anisotropy in zirconium and zirconium base alloys. Journal of ASTM International 2, JAI12945.

Tresca, M.H., 1878. On further applications of the flow of solids. Journal of the Franklin Institute 106, 326-334.

Walley, S.M., 2007. Shear localization: A historical overview. Metallurgical and Materials Transactions A-Physical Metallurgy and Materials Science 38A, 2629-2654.

Williams, J.C., Baggerly, R.G., Paton, N.E., 2002. Deformation behavior of HCP Ti-Al alloy single crystals. Metall. Mater. Trans. A 33, 837-850.

Wright, T.W., 2002. The Physics and Mathematics of Adiabatic Shear Bands. Cambridge University Press, Cambridge.

Wright, T.W., Ockendon, H., 1996. A scaling law for the effect of inertia on the formation of adiabatic shear bands. International Journal of Plasticity 12, 927-934.

Xue, Q., Meyers, M.A., Nesterenko, V.F., 2002. Self-organization of shear bands in titanium and Ti-6Al-4V alloy. Acta Materialia 50, 575-596.

Zener, C., Hollomon, J.H., 1944. Effect of strain rate upon plastic flow of steel. Journal of Applied Physics 15, 22-32.

Zhang, Z., Cuddihy, M.A., Dunne, F.P.E., 2015. On rate-dependent polycrystal deformation: the temperature sensitivity of cold dwell fatigue. Proceedings of the Royal Society A 471 20150214.

Zhou, M., Ravichandran, G., Rosakis, A.J., 1996a. Dynamically propagating shear bands in impact-loaded prenotched plates .2. Numerical simulations. Journal of the Mechanics and Physics of Solids 44, 1007-&.

Zhou, M., Rosakis, A.J., Ravichandran, G., 1996b. Dynamically propagating shear bands in impact-loaded prenotched plates .1. Experimental investigations of temperature signatures and propagation speed. Journal of the Mechanics and Physics of Solids 44, 981-1006.